National Aeronautics and

Space Administration

# Lunar Crater Observation and Sensing Satellite (LCROSS)

## Instrument Calibration Summary

## Version 1

### APRIL 9, 2010

Authors: Kimberly Ennico, Anthony Colaprete, Mark Shirley, Diane Wooden

Kimberly.Ennico@nasa.gov

# 1   LCROSS Payload Overview

The LCROSS Payload consists of nine science instruments, their supporting electrical, mechanical and optical harnesses, a central data handling unit (DHU) assembly, and thermal hardware (heaters, thermistors, and thermostats), all assembled onto the LCROSS spacecraft R6 Radiator Panel as shown in **Figure 1.** Eight of the nine science instruments are configured with their apertures in the +X direction (spacecraft body frame/SBF) and are accommodated in the Payload Observation Deck (POD) as shown in **Figure 2**. The ninth instrument, near infrared spectrometer #2 (NSP2), has its entrance optical element orientated in the –Z direction (spacecraft body frame/SBF). The Payload is located on the inboard side of the LCROSS spacecraft R6 Panel and integrated with the LCROSS Spacecraft as shown in **Figure 3**. The LCROSS payload instruments (**Figure 4**) are briefly described below.
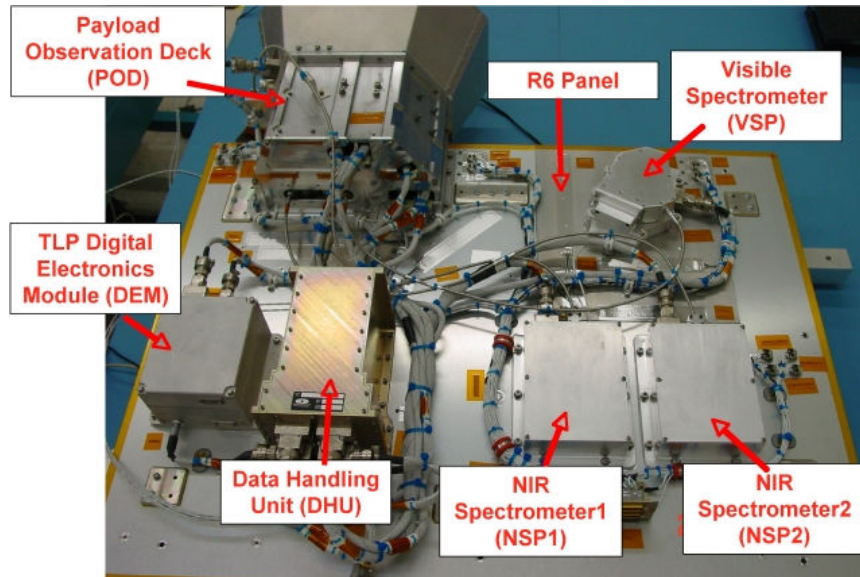

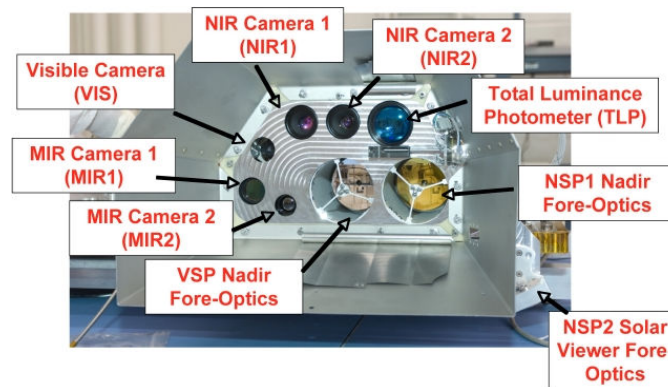
**Figure 1.  LCROSS payload on the R6 Panel.**



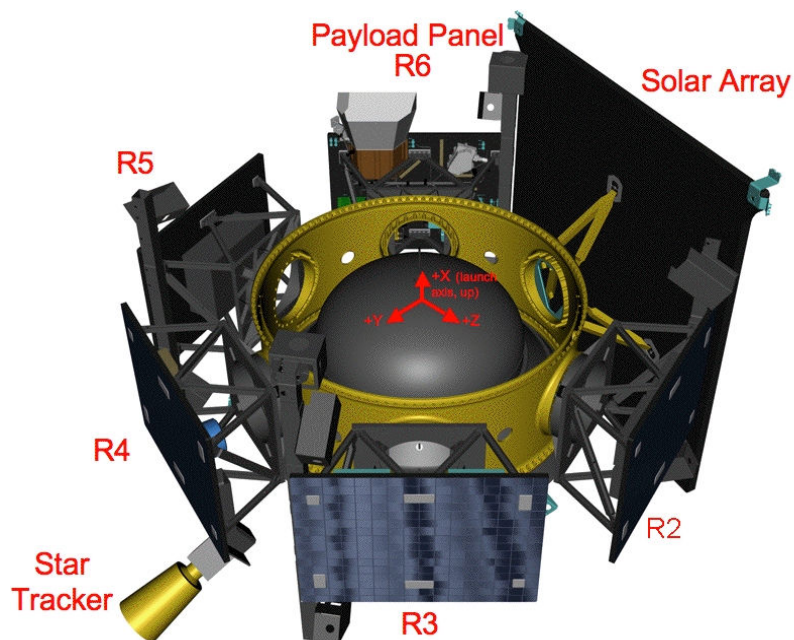**Figure 2.  Payload Observation Deck (POD).**

**Figure 3. LCROSS payload location on the LCROSS space vehicle.**
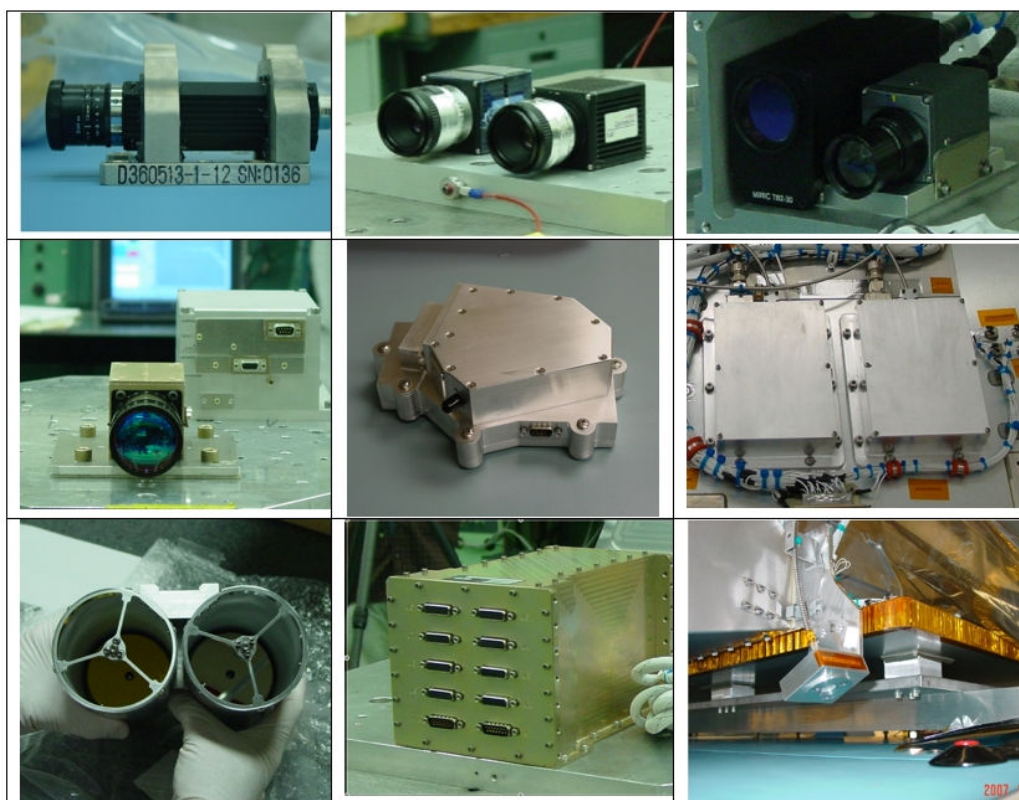


**Figure 4. The LCROSS payload instruments. Top Row: VIS, NIR1 & NIR2, MIR1 & MIR2. Middle Row: TLP, VSP, NSP1 & NSP2. Bottom Row: Nadir Fore-Optics, DHU, Solar-Viewer Fore-Optics.**

**Visible Camera.** The LCROSS visible camera (**VIS**) is a ruggedized analog video camera from the RocketCam™ camera family developed by Ecliptic Enterprises, Inc. The unit consists of a camera module and a lens. The camera's focal plane CCD sensor is 752 [H] x 582 [V] pixel format, operating at 30 Hz (60 fields/sec). The flight unit's lens is a 12 mm (focal length), f/1.2 lens providing a 30.1 deg [H] x 22.8 deg [V] (37.8 deg [Diagonal]) field-of-view. Interlaced NTSC fields are sampled by the Data Handling Unit (DHU) at 720 x 243 resolution resulting in a final image resolution of 720 x 486 pixels. Each pixel is 24-bit RGB with 8 bits per color channel. These images are compressed using a lossy compression algorithm performed by the Analog Devices 611 Video Codec set on 80% quality and decompressed on the ground. The LCROSS visible camera contains no cryogenic liquids or moving parts. The visible camera's peak power during operation is 2.9 W. The visible camera has been fixed to an auto-gain/white balance setting.

**Near-Infrared Cameras.** The LCROSS payload contains two near infrared (IR) (0.9-1.7 μm) cameras (**NIR1/NIR2**). Each camera consists of a Goodrich Sensors Unlimited model SU320-KTX and a CCTV lens. Each camera's focal plane InGaAs sensor has a 320 [H] x 240 [V] pixel format. The 25 mm, f/1.4 C-mount glass lens provides a 28.7 deg [H] x 21.7 deg [V] (36.0 deg [Diagonal]) field-of-view. Although the camera's native format provides 320 [H] x 240 [V] 12-bit images, the images are converted within the camera to an analog NTSC signal before transfer to the DHU where they are captured at 720 [H] x 486 [V]. Due to similar processing within the DHU as needed for the VIS images, the two NIR camera images are captured as 24-bit per pixel RGB. Because the NIR cameras provide grayscale images, the three RGB channels are identical except for noise introduced in the conversion to and from NTSC. These images are compressed in the DHU using a lossy compression algorithm performed by the Analog Devices 611 Video Codec set on 80% quality and decompressed on the ground. In addition to a camera body and a lens, near infrared camera #1 (NIR1) also contains a long-pass filter (λ > 1.4 μm). NIR2, in comparison, is filter-less. Lenses for both cameras were provided by UkaOptics (http://www.ukaoptics.com/ #2514M) as part of the standard Goodrich package. These lenses are not optimized for the IR. The IR throughput of the lenses has not been documented, but is expected to be ~40%. The near-infrared cameras contain no cryogenic liquids or moving parts. There is an internal thermo-electric cooler that actively cools the InGaAs sensor. The manufacturer default settings for this cooler are used. Each camera's peak power during operation is 1.6 W. Both gain and exposure times are configurable by commands sent to the camera.

**Mid-Infrared Cameras.** The LCROSS payload contains two mid-infrared (MIR) (6.0-13.5 μm) cameras (**MIR1/MIR2**). Mid-infrared camera #1 (MIR1) is a ruggedized vanadium oxide (VOx) microbolometer MIRIC® TB2-30, from Thermoteknix Ltd. Mid-infrared camera #2 (MIR2) is model ThermoVision Micron from Flir Systems/Indigo Operations. Each camera's uncooled microbolometer focal plane sensor has a 164 [H] x 128 [V] pixel format and is digitized at 14-bit resolution. Each camera has a 30 mm, f/1.6 lens providing a 15.0 deg [H] x 11.0 deg [V] (18.6 deg [Diagonal]) field-of-view. MIR1 also contains a 6-10 μm bandpass filter. MIR2 is filter-less. MIR1 is backfilled with dry Argon gas to prevent degradation due to humidity for terrestrial applications and does not contain any component volatile in vacuum. Internal to both MIR modules is an instrumented-motorized shutter to provide a reference for temperature measurements. Each camera's peak power during operation is 1.3 W. A camera gain, which determines the sensitivity to temperature scenes

(high gain: -20 ºC < T < +150º C, low gain: +150 ºC < T < +500 ºC), is configurable with a command sent to the camera.

**Total Luminance Photometer.** The Total Luminance Photometer (**TLP**) provides visible light (400-1000 nm) intensity data at a 1000 Hz sampling rate. The TLP instrument consists of two elements: (1) the Sensor Electronics Module (**SEM**), which contains the optics and sensor assembly and signal filtering, and (2) the Digital Electronics Module (**DEM**), which converts the analog sensor signal to a digital output, as well as higher order functionality. The DEM is a commercial package that was modified for LCROSS. This instrument is designed and manufactured by NASA Ames Research Center. The optics in the SEM delivers an unobstructed ~10 degree diameter field-of-view. The TLP's sensor element is an uncooled Advanced Photonix, Inc. (API) avalanche photo diode (APD) packaged in a dry-air sensor container that can operate in a vacuum. The TLP SEM is connected by an electrical harness to the TLP DEM. The SEM and DEM are located within the Payload Observation Deck (POD) and on the R6 Panel, respectively. The DEM is interfaced with the DHU (also on the R6 Panel) via a second cable, from which it is controlled. The SEM and DEM's peak power during operation are 2.5 W and 12.0 W, respectively.

**Visible Spectrometer.** The LCROSS visible spectrometer (**VSP**) is a modified-commercial model from Ocean Optics Ltd., with its core operation based on their COTS QE65000 model. It has been adapted for space use and is of similar design to a recently delivered spectrometer to Los Alamos for a Mars Science Laboratory (MSL) payload for launch in 2011. The VSP spectrometer design consists of an FC optical fiber input (0.11 NA) feeding a 25 micron x 1 mm entrance slit, where light is diffracted by a 1-inch f/4 optical cross Czerny-Turner spectrometer (grating 600 lines/mm, blazed at 350 nm) with an oversized camera mirror. The ~263-650 nm spectrum from the slit is imaged onto a 1044 x 64 pixel Hamamatsu CCD detector. The data is co-added within the spectrometer, delivering a 16-bit, 1 x 1044 pixel spectra to the DHU electronics for packaging. The first 1024 pixels contain spectral data. The remaining 20 pixels contain provide temporally coincident but off-slit dark reference pixels. The VSP resolving power is R~300, 500, and 850 at 300, 400 and 600 nm, respectively. The VSP contains no moving parts. The CCD detector is cooled by an internal Thermoelectric Cooler (TEC), whose set point is programmable. The VSP power is 4.8 W (TEC off), and can reach 11.8 W (at TEC setting -10° C at operating temperature +19-20° C). Integration time (between 8 ms and 65.5 s) is configurable. Additionally, the VSP supports two operation modes – single and bracket spectra. The former is a single spectra acquisition of the appropriate requested integration time. The latter is a three-spectra acquisition defined by a base integration time and a multiplier that is divided or multiplied by the base integration time to yield a shorter or longer exposure time, respectively. The VSP is fed by a 75 cm length 600-micron core-diameter UV/Vis glass fiber attached to a fore-optics unit in the POD. This fore-optics unit (see below) is a fixed two-mirror and one lens system designed to provide a one degree diameter field-of-view.

**Near-Infrared Spectrometers.** The LCROSS payload contains two near-infrared spectrometers (**NSP1**/**NSP2**), located on the R6 Panel. Their electronics units are identical, but they have different fore-optics designs. Near infrared spectrometer #1, NSP1, also known as the **nadir** NSP, is located inside the POD and its aperture is positioned in the +X direction (spacecraft body frame/SBF). Near infrared spectrometer #2, NSP2, also known as the **solar-viewer** or occultation NSP, has its wide-field aperture centered along the -Z

direction (spacecraft body frame/SBF). Both spectrometers provide 1.20-2.45 μm spectral coverage and nominal resolution 0.035 μm/pixel, yielding resolving powers R ~ 37-65 (NSP1) and R ~ 36-77 (NSP2). Both spectrometers are manufactured by Polychromix, a company whose primary spectrometer line is designed for material analysis and chemical sensing. The spectrometers are designed to take a single SMA NA=0.22 fiber as input instead of a slit, whose diameter defines the instrument resolution. Since each spectrometer contains a single TEC-cooled InGaAs sensor element, a 1D-spectrum is created using an innovative electronically-tunable MEMS device that spatially masks the dispersed spectrum within the instrument. This series of masks undergoes a digital transform on the ground to recreate the spectral information. The spectrometer contains no moving parts (excluding the MEMS chip) and the peak power for each NSP is 2.5 W. NSP1 and NSP2 are each fed by a single 600-micron core-diameter low-OH glass fiber of length 75 cm and 1.45 m, respectively, attached to a fore-optic. The NSP1 fore-optics unit (see below) is located within the POD and is a fixed two-mirror and one lens system designed to provide 1 degree diameter field-of-view. The NSP2 fore-optic (see below) is a diffuser providing ~130° field-of-view, and is located external to the POD housing. Both spectrometers have three modes, Impact **Flash** (IF), **Hadamard** Spectrum (HS) and **Diagnostic** Mode (DM), which are configurable by sending a command to the units.

**Fore-Optics and Fibers.** The LCROSS payload contains two fore-optic units and three fibers. The three single-core fibers connect the electrical units of the three LCROSS spectrometers to their respective fore-optics (i.e., light-gathering optics). All fibers are manufactured by Fiberguide Industries. The two fore-optics, a dual-scope fore-optic feeding the NSP1 and VSP spectrometers and a diffuser fore-optic feeding the NSP2 spectrometer, have been designed specifically for the LCROSS mission by Aurora Technologies. The dual-scope fore-optic provides 1 degree diameter field-of-view (per scope) and a separation between the two scopes of < 0.1 degrees. The diffuser fore-optic provides an unattenuated ~130° field-of-view. The fibers were chosen to optimize for the band-pass and be compatible with the throughput and entrance optic requirements by the spectrometers. For the VSP, the fiber is a 75 cm SuperguideG UV/VIS Spectral Range with NA=0.12+/-0.02. For the NSPs, the fibers are AnhydroguideG Low OH fibers with NA=0.22+/-0.02, with lengths 75 cm and 145 cm for NSP1 and NSP2, respectively. All three fibers have 600 μm core-diameters and are encased in a 1/8 inch (ID) stainless steel monocoil for ruggedization.

**Data Handling Unit.** The LCROSS Data Handling Unit (**DHU**) is a ruggedized video camera controller and data handling system based on the ruggedized Digital Video Systems (DVS) developed by Ecliptic Enterprises, Inc. It captures and transmits compressed digital spectrometer, video and photometric data telemetry (in CCSDS format) from all nine instruments from the LCROSS science payload. The DHU is a single conduction-cooled chassis designed to operate as independently as possible from its host vehicle. In the limiting case, DHU operation is completely self-contained except for activation/deactivation commands that originate from the ground. The DHU can store up to 10 slots of Non-Volatile Memory (NVM), which can be used for sequencing power and operational commands to the science instruments. The DHU contains no moving parts, operates from the 32 V power supply by the spacecraft power bus, and its peak power during operation is 13.5 W. The DHU also provides the time-stamping function of all the science instruments and itself and provides error logs for when science data frames are dropped or corrupted due to bandwidth or performance issues.

## 2   Payload Alignment

The center of the nadir near-infrared spectrometer (NSP1), with its 1 degree diameter field of view (FOV), is defined as the payload boresight, to which all instruments centers/edges are referenced. This is ~+X (launch) axis in spacecraft body frame (SBF) (**Figure 5**). The visible spectrometer's (VSP) FOV overlaps NSP1. The solar viewer near-infrared spectrometer (NSP2) is orientated within a few degrees from the –Z axis (SBF).
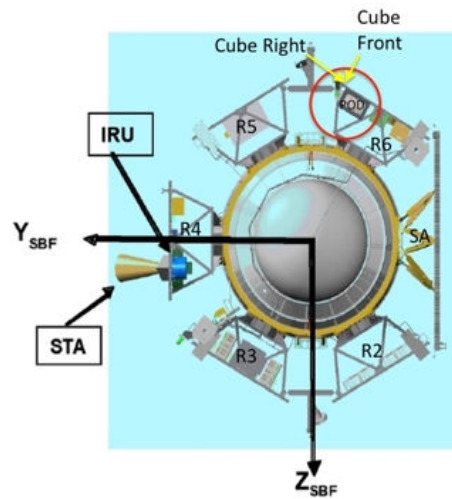


**Figure 5.  LCROSS spacecraft body frame (SBF) coordinate system. +X is the launch axis.**

To measure the NSP1 boresight after launch, there were seven limb crossings observed by the VSP & NSP1 on lunar swingby DOY 09-174. LCROSS swept the instruments across the lunar limb at two points, roughly 90 degrees apart.  LCROSS slewed at 0.2°/sec, during which spectra from the nadir spectrometers (VSP & NSP1) were taken continuously at 0.5 Hz and 71 Hz, respectively.  The spectrometer boresights were estimated by normalizing the actual signal and comparing it against a predicted signal generated by: (1) guessing a boresight vector (and therefore FOV) relative to the Star Tracker, and (2) computing the percentage of the FOV filled by moon vs. empty space by computing the geometric intersection of the moon's disk with the FOV.  An algorithm searched through possible boresight vectors, minimizing the root-mean-square error between the predicted and actual signals.  The largest source of error in this approach was time synchronization between the ground, spacecraft and instruments. The NSP1 post-launch measured boresight in S/C coordinates is $\{X,Y,Z\}_{SBF}$ = {0.99987989, 0.00680375, 0.01392503}. This was 0.06 +- 0.02 delta-degrees from pre-launch boresight. Subsequent Earth calibration crossings, when the Earth underfilled the spectrometer FOVs, provided additional gross checks, but were at a lower fidelity than the lunar limb data.

To illustrate the relationship between the visible camera (VIS) and the nadir near-infrared spectrometer (NSP1), **Figure 6** shows a flight image from the VIS camera (in the image entitled 'OverlayForm') arranged in orientation to match the STK (Satellite Toolkit) planning tools, with the 1° dia. NSP1 FOV calculated from the pre-launch and measured on-orbit boresight in orange and red, respectively. The green dot is an estimate of the impact location, within 100m of the impact, at the time this analysis was performed, showing that

the NSP1's FOV did encircle the impact point (this is also substantiated with detection in the flash mode) and correlates with the ejecta cloud detected a few seconds later in the VIS camera. For the image shown in Figure 6, the ejecta cloud is underfilling the NSP1 FOV.

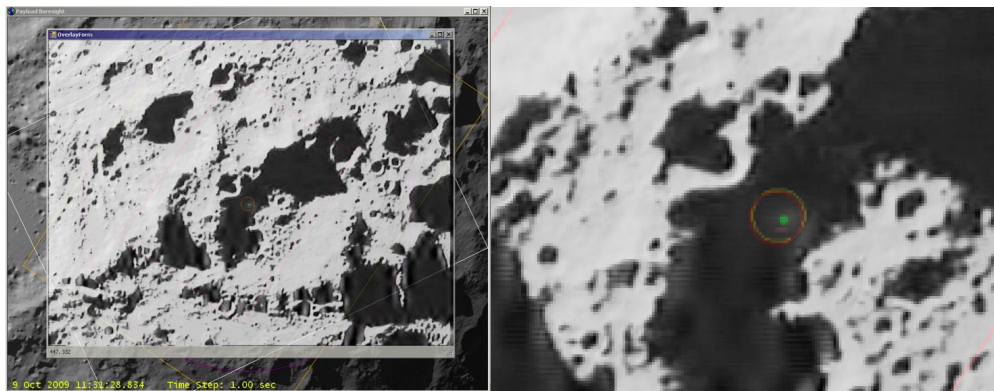| Table 1.  NSP1, VSP & NSP2 Boresights in SBF. | | | |
|---|---|---|---|
| | X | Y | Z |
| NSP1 pre-launch | 0.999879 | 0.00794955 | 0.0133901 |
| NSP1 on-orbit | 0.99987989 | 0.00680375 | 0.01392503 |
| NSP2 pre-launch | 0.00175365 | -0.141368 | -0.994075 |
| NSP2 on-orbit | Not measured | | |
| VSP pre-launch | 0.999877 | 0.008528 | 0.013176 |
| VSP post-launch | Not calculated from the data | | |



**Figure 6. (left) Overlay of VIS flight image near time of impact with predicted location and geometry of the NSP1 1° dia. boresight (red: pre-launch; orange: post-launch). (right) Zoomed in area.**

# 3   VIS Calibration

The visible cameras (VIS) provided context information about the scene at visible wavelengths. It had the largest field of view among all the cameras. The data files produced by the VIS, transferred to the DHU, and unpackaged by the GSEOS program are 720 [rows] x 486 [column[ pixel 2D images, with three 8-bit [0-255 DN] channels representing a RGB color assignment. Each image has NSTC artifacts that typically affect columns 0-3 & 712-719, and rows 0 & 485.  If desired, to generate a grayscale image of the RGB pattern, the following algorithm (NTSC standard) can be used: gs = 0.2989*bmpR + 0.5870*bmpG + 0.1140*bmpB, where bmpR, bmpG, bmpB are the raw DN values for the R, G, and B channels, respectively.

The camera was configured at fixed f/1.2 aperture, AGC (automatic gain control) "on", and white balance "auto." At this configuration, the limiting sensitivity is 3 lux. The camera demonstrated blooming on scenes when more than half of the pixels observed dark (no light) with a bright object in the field of view. This is seen immediately in all the LCROSS Earth calibration images, when the Earth would subtend a very small fraction of the FOV and during the lunar swingby limb measurements, when the bright Moon was positioned such that most of the field was dark sky. The inability to control or query the gain and exposure settings prevented radiometric calibration of the images.

# 4 NIR1/2 Calibration

The data files produced by the NIR1 & NIR2 transferred to the DHU, and unpackaged by the GSEOS program are 720 [rows] x 486 [column] pixel 2D images, with three 8-bit [0-255 DN] channels representing a RGB color assignment. The NIR camera is only capable of generating grayscale images and the R channel is used as the data value. The two remaining channels are within +/- 2 DN (data numbers) of each other for a constant illumination or dark scene, whose cause is due to noise introduced in the conversion to and from NTSC. Each image has NSTC artifacts that typically affect columns 0-4 & 710-719, and rows 0-6 & 482-485. The edge effects for both NIRs were more pronounced than what is seen in VIS, particularly along horizontal edge rows.

NIR1 is slightly out of focus. This was a known issue pre-launch.

The NIR cameras have configurable gain and exposure times. All images were set at digital Gain=1 to maximize dynamic range within the narrow 8-bit (0-255 DN) analog camera output. Values > 220 DN are in the non-linear/near-saturation region and are not considered valid data. Values < 20 DN are below the average dark current value (~23 DN across the image) and are considered not useable. These latter points tend to be NTSC artifacts. The NIR cameras demonstrated strong blooming around saturated pixels that quickly spread across the whole image.

The NIR camera exposure time was changed by adjusting the camera OPR (Operational Configuration) setting. The mapping of OPR to exposure time in milliseconds is summarized in Table 2. Changing OPR also changed an internal gain setting, therefore images with 2x integration time do not have 2x detection of photons. This is shown by a series of curves for a fixed illuminated flat field scene provided by a NIST calibrated tungsten bulb sphere in Figure 7. The OPR setting is configurable by a command sent to the camera and recorded in the flight telemetry.

In flight, the NIR cameras were set at autogain for the lunar swingby images, where the half-dark/half-light scene saturated the images. Calibration opportunities using the Earth provided targets for evaluating the OPR settings. Low OPR values (2-4) provide non-saturated images for Earth scenes. In the final hour of the mission, NIR1 and NIR2 were set for OPR 7 and OPR 5 to stay within the linear range of the NIR camera response for the south pole scene. NIR2 was later adjusted to OPR 10 in the final few frames of the mission when the camera was staring at the bottom of the Cabeus crater.

An absolute radiometric calibration was not performed on the two flight near-infrared cameras. A flight spare camera was tested in both configurations (including a flight spare 1.4 µm long-pass filter for NIR1). The test provided a "best effort" radiometric calibration for the flight units. In this test, the camera recorded the values from a NIST-calibrated integrating sphere, whose flux was attenuated by external IR neutral density (ND) filters, for a range of OPR settings. The images where >95% of the pixels were within the valid 20-200 DN data range were used as the flat field for that OPR. The example for the unfiltered camera (NIR2 configuration) for OPR4 with OD0.6 (external filter) is shown in Figure 8. The in-band radiance is the integration of the known NIST Sphere Radiance [W/m^2 µm

sr] * %T (for all filters in system including internal NIR1 filter for NIR1) over λmin= 0.95 to λmax = 1.7 μm.

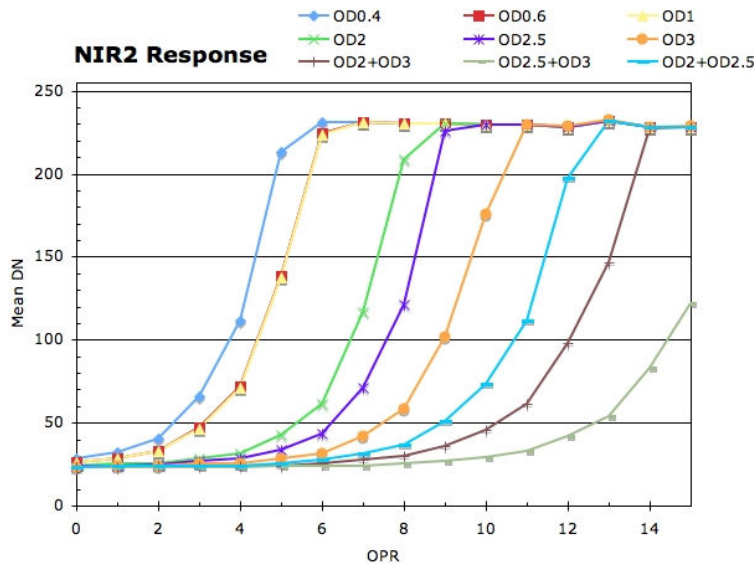| Table 2. NIR OPR vs. exposure time. | | | |
|---|---|---|---|
| OPR | Exposure Period Count | Exposure Time (ms) | Nominal FPA Sensitivity (e/count) |
| 0 | 672 | 0.11 | 22000 |
| 1 | 1008 | 0.17 | 16000 |
| 2 | 1344 | 0.22 | 9600 |
| 3 | 1680 | 0.28 | 5000 |
| 4 | 2688 | 0.44 | 3700 |
| 5 | 3696 | 0.61 | 2200 |
| 6 | 5040 | 0.83 | 1400 |
| 7 | 7056 | 1.16 | 850 |
| 8 | 9744 | 1.60 | 520 |
| 9 | 13440 | 2.20 | 320 |
| 10 | 18816 | 3.08 | 200 |
| 11 | 26208 | 4.29 | 120 |
| 12 | 36624 | 6.00 | 75 |
| 13 | 51072 | 8.37 | 46 |
| 14 | 70896 | 11.61 | 28 |
| 15 | 99120 | 16.24 | 18 |



**Figure 7. Mean DN for NIR Camera (no internal filter) vs. OPR for a series of external neutral density filters to attenuate the illumination from a fixed source (NIST Sphere).**

To relate DN to an integrated radiance (W/m^2 sr), the following algorithm was used:

1. Mask values <20 DN and > 200 DN as 'bad'. Assign them NaN.
2. Subtract a 2D dark image (from the dark library) with the same OPR setting.
3. Divide this dark-subtracted image by the Flat Field image for that OPR derived from the NIST data set.

**Figure 8. Unfiltered (NIR2 configuration) OPR 4 (ND0.6) camera image of NIST Sphere illumination.**

An example of applying the radiance calibration to images during EarthCal1 DOY09-213 for NIR1 at OPR 4 & 6 and NIR2 for OPR 3 & 4 is shown in Figure 9. For the histograms, subarray box 35x35 was chosen to subtend within the circular earth (analysis was not repeated for a circular aperture). The mean values calculated for different OPRs for the same scene (illuminated Earth) are within 20% of each other. A comparison with a mid-latitude uniform albedo SBDART model confirmed our levels to better than 50%, with the knowledge that there were large variations within our Earth images that are not addressed by the SBDART mode. Comparison to a model that includes cloud cover and illumination on the day/time the LCROSS images were taken is the next step.
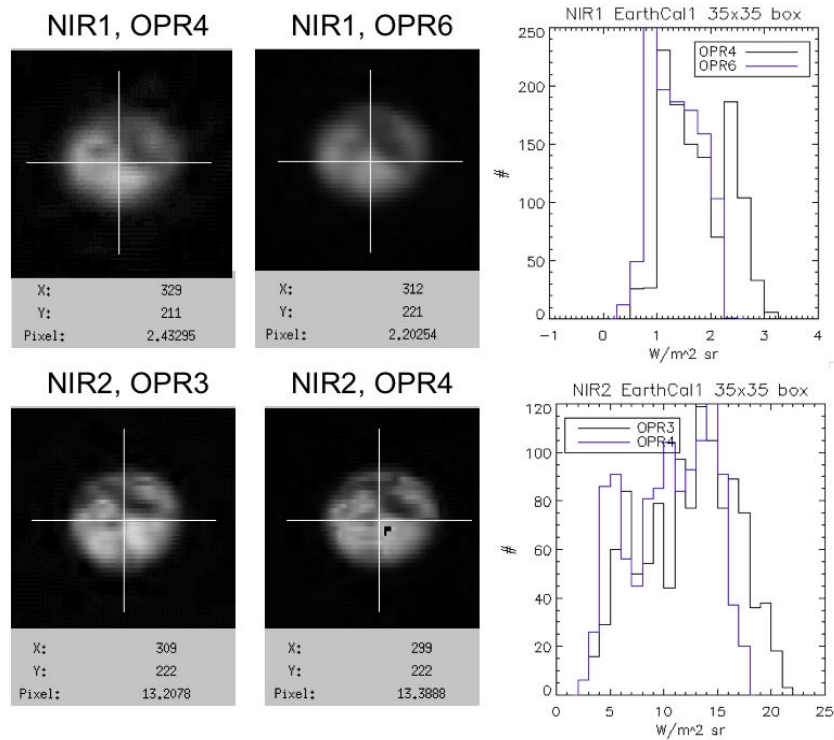


**Figure 9. Earth calibration images for NIR1 & NIR2, each at two OPR settings after applying radiance calibration (with saturated pixels flagged with NaN, appear black in NIR2).**

# 5 MIR1/2 Calibration

The data files produced by MIR1 and MIR2, transferred to the DHU, and unpackaged by the GSEOS program are 160 [H] x 120 [V] pixel 14-bit [0-16383] 2D images.

MIR2 is slightly out of focus. This was a post-launch anomaly. The focus stayed at this new position throughout the 112-day flight mission. The MIR2 defocus can be corrected using a PSF de-convolution using single-pixel Moon images from the MIRLOOKdata collection period.

Both cameras demonstrate large angle distortions similar to pincushion. Image distortion correction was not performed on the data. The high-quality MIR lunar images (i.e., warm peaks and cold basins) provide sufficient sample shapes to remove the distortion.

The cameras are expected to differentiate -20 °C (253 K) and +500 °C (773 K). There are two settings: high (Hi) and low (Lo) Gain. These are optimized for -20 °C < T < +150 °C (253 K < T < 423 K) and +150 °C < T < +500 °C (423 K < T < 773 K), respectively . The nominal gain used in flight was "Hi Gain." "Lo Gain" was used in early calibration sequences near power-on for testing gain change commands.

The units were programmed to perform a flat field correction (FFC) every two minutes. Flat field correction is the process of measuring the output and creating an offset for every pixel so that the output becomes totally uniform (i.e., flat). The correction is requested when a uniform temperature internal shutter covers the entire field of view. This is the recommended mode of operation for these cameras.

Pre-launch thermal vacuum data indicated that MIR camera response to a fixed scene will drift with time. This is common to both cameras for <600 s from power on, but MIR2 will continue to drift for up to 50 minutes after power on. To illustrate this, **Figure 10** shows the first 20 minutes after power on for MIR1 and MIR2 for three data sets take at vacuum. Two are from flight, one is from thermal vacuum testing in May 2008. The mean value for the entire image is plotted, whose absolute value is strongly dependent on the scene (e.g., moon filling scene as in pre-impact/impact or empty sky like in starfield or separation), and thus an offset is added to bring all three onto the same scale for a comparison with time. Because the scene was not changing spatially (and not expected to be changing thermally either) the mean camera response should be flat, with the occasional artifacts due to FFC every two-minutes. MIR1 demonstrates a transient response within the first 600s after power on. The FOVs of the two cameras overlap sufficiently that both cameras should respond to the scene in a similar manner. The longer-time temporal drift in MIR2 response is an issue for providing a valid calibration to temperature for flight data sets, particularly at early time since power on.

The temperature calibration of the flight MIR images were derived from a comparison with a *thermal model* provided to the LCROSS science team from the LRO Diviner team, for the lunar south pole at the day and time of the LCROSS impact (DOY09-282, 11:31 UTC). This model takes into account the emissivity of the lunar solar reflectance and has been validated against actual Diviner measurements. For temperatures below 200 K and above

350 K, the model agrees with Diviner flight data to +/-2K and +/-5K, respectively.[1] Sub-arrays were chosen "by hand" to sample the temperature from the model (in degrees K) and match with the LCROSS raw MIR1/MIR2 DN (data numbers). Twenty-six and twenty-seven areas were chosen for MIR1 and MIR2, respectively.
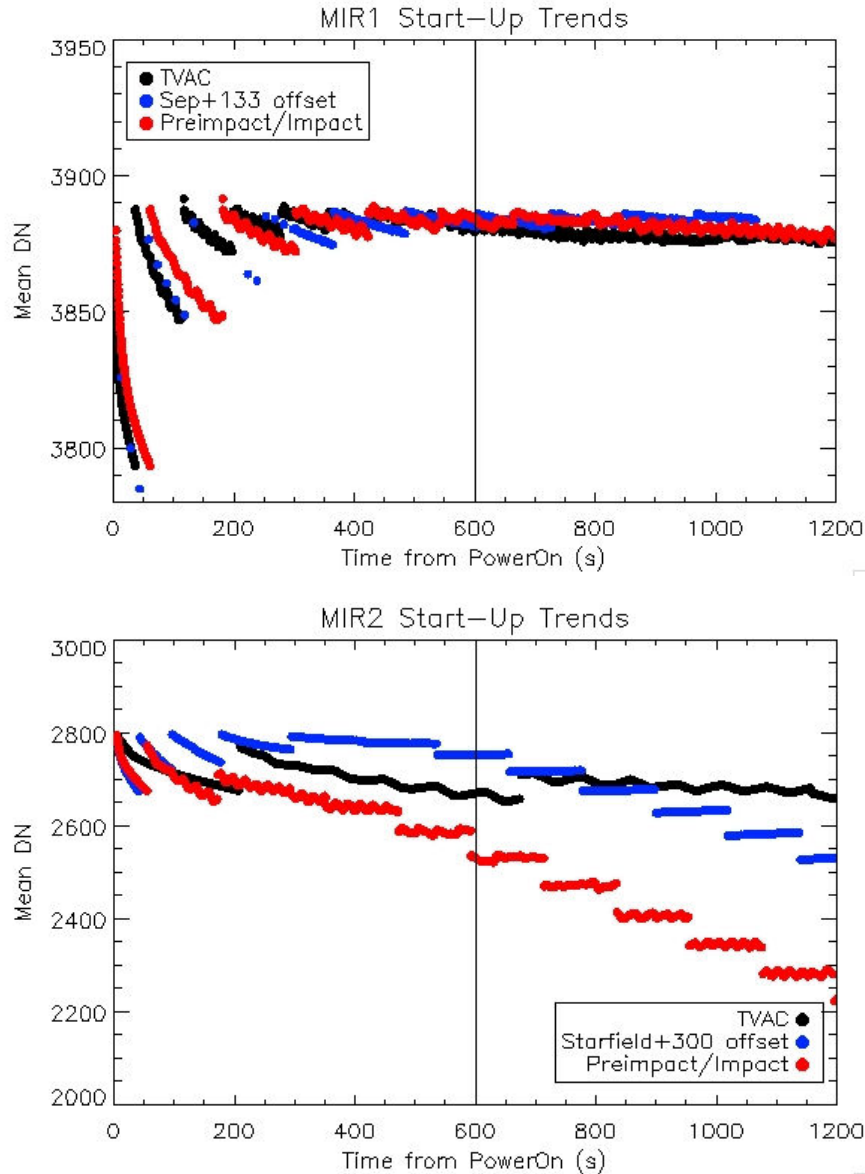


**Figure 10. Mean value of entire image (scene will affect overall level) for first 20 minutes for vacuum data for (a) MIR1 and (b) MIR2. The discrete jumps are due to flat field corrections occurring every 120 seconds. The vertical line is placed at 600s from power on, where the MIR1 data flattens in response (with a constant scene). The MIR2 image continues to drift.**

---

[1] Source: Diviner PI, David Paige assessment of model submission to Tony Colaprete at the time of this memo.

A comparison for the Diviner model and the MIR2 image and the 27 selected points (black dots) at time of flash is shown in **Figure 11**. It should be noted that these 26(27) sampled areas specifically *do not* include data from the coldest regions (<220K), for which the camera's low temperature performance is most uncertain. The white dots are 20 areas sampled in the coldest regions to provide knowledge of the lowest temperature sensitivity limit for the MIR cameras. MIR1 and MIR2 consistently could not distinguish values <125 K mapping to lowest recorded DN values ~3799 DN and ~1500 DN, respectively. Around the edges of the cold crater basins, there are small numbers of pixels with Diviner thermal model 125-220K temperatures, for which analysis of seven regions was attempted but with inconsistent one-to-one mapping to DN for the cameras.
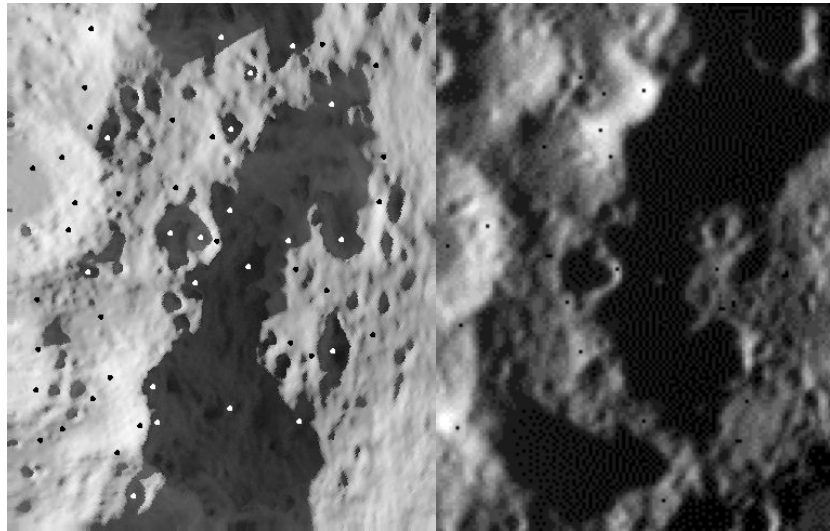


**Figure 11. (a) Diviner thermal model image in greyscale, where values are in Kelvin. (b) MIR2 image at time of impact. The black dots represent 27 sample points used for the main one-to-one mapping. The white dots are 19 sample points in the "low temperature" regime to investigate sensitivity limits that are not used in the fits. A similar mapping was performed for MIR1 (not shown here).**

The comparison to the Diviner data plus an anchor point at 415 K (which is present in swingby images) provides a translation from DN to temperature (in degrees K) by the polynomials summarized in **Table 3**. The fit with the high tie point is used in the PDS 2010-03-17 delivery. Due to the transient effect mentioned above, this calibration is best valid at the time of impact (3000s after power-on).

| Table 3. Two fits for temperature calibrations of the MIR flight camera datasets. $y[Temp\ K] = a0 + a1*x + a2*x^2; x=[DN]$; to derive deg C, subtract 273.15 from answer. | | | | |
|---|---|---|---|---|
| | MIR1 "Diviner Fit" | MIR1 "Extended Fit" | MIR2 "Diviner Fit" | MIR2 "Extended Fit" |
| Valid Range | [3839:4170] | Deliberate tie point 4500 DN = 410 K | [1749:3218] | Deliberate tie point 5200 DN = 410 K |
| a0 | - 1.0910E+04 | - 4.2278E+03 | - 2.0993E+02 | - 1.9222E+01 |
| a1 | + 5.2863E+00 | + 1.9303E+00 | + 3.2670E-01 | + 1.6248E-01x |
| a2 | -6.2120E-04 | -2.0009E-04 | -4.9696E-05 | -1.5496E-05x2 |
| R^2 | 9.7390E-01 | 9.7640E-01 | 9.6687E-01 | 9.6631E-01 |

To adjust for the MIR2 response drift, a first-order correction was made to the MIR2 dataset before applying the temperature calibration defined above. This correction was derived from

pre-launch thermal vacuum performance data where the scene's (POD cover) mean temperature was constant (MIR1 data supports this) and normalized to the mean MIR2 DN value in the flight impact image. Figure 12 shows the mission's final hour mean MIR2 data (black) and the response "drift corrected" derived from two thermal vacuum data sets (blue & green). The offset correction (which is a function of time from power on) was adopted from CPT1 (blue curve) because it gave a mean response during final hour with a shape similar to MIR1. The fit parameters used to create this "offset" are summarized in Table 4.
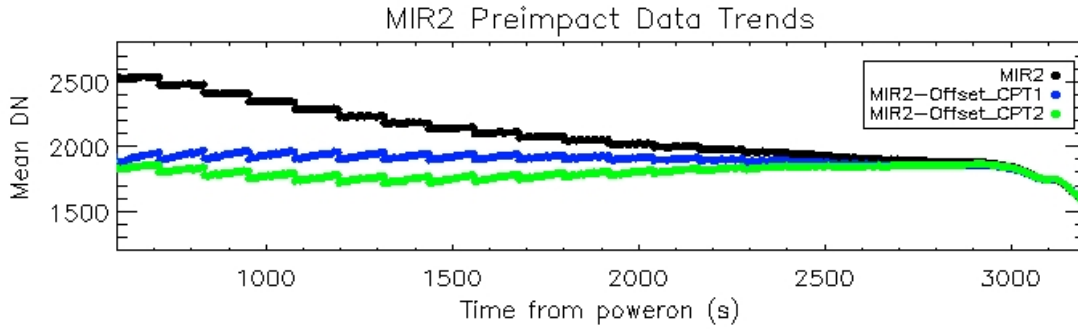


**Figure 12. The effect of subtracting a correction with time to MIR2 based on TVAC test data (two sets shown. The blue curve is the one used for the temperature calibration.**

| Table 4. MIR2 Drift Correction | |
| --- | --- |
| Offset[t] =m0+m1*(x)+m2*(x^2)+m3*(x^3)+m4*(x^4); t= time in seconds since power-on | |
| MIR2[DN,time] – offset[t] = MIR2'[DN,time] | |
| a0 | 1.138700E+03 |
| a1 | -9.225100E-01 |
| a2 | 1.837200E-04 |
| a3 | 3.098900E-08 |
| a4 | -1.047500E-11 |

For the final hour data set, this temporal correction is first subtracted from the raw MIR2 DN data and next converted to temperature. The resulting comparison of the mean temperature for MIR1 & drift-corrected MIR2 is shown in Figure 13. The overall mean offset is due to the contribution of pixels with temperatures < 220 K which have ~30 K errors (see below). This correction has not been optimized and the largest discrepancies are at the earliest times. There are also residual issues (~10 K) due to the FFC that are not addressed with this simple drift correction.

An example of applying the temperature calibration to MIR images at time of impact is shown in Figure 14. Here, both images are shown on the same linear color scale (min=225K, max=350K). The cursor is placed at the highest temperature location. Figure 15 extends the performance down to 125 K, where the discrepancies the low temperature assessments (< 220K) between the cameras are shown. The large spike in each histogram are the values for cold crater basins, where average values for MIR1 and MIR2 are 210 K and 190 K, respectively. Therefore with this calibration temperatures < 220K have ~30 K errors.
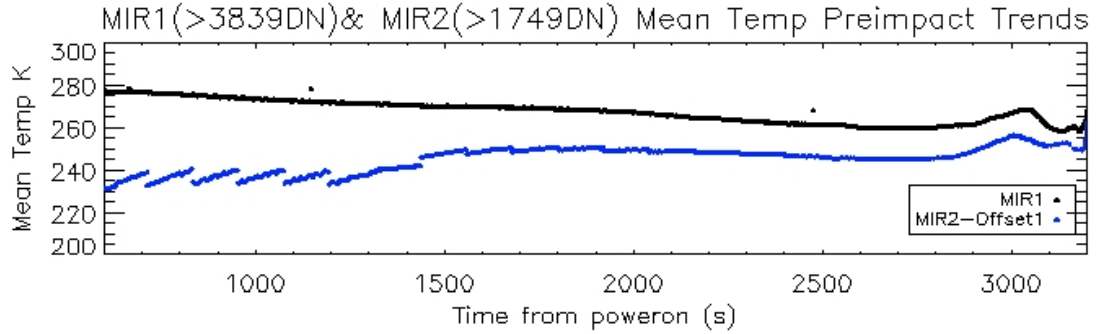
**Figure 13. The mean temperature for MIR1 and MIR2 (after applying a drift correction), for pixels with original raw values >3839 DN and >1749 DN for MIR1 and MIR2 respectively, where temperature calibration is valid. The drift correction is less constrained at earlier times.**
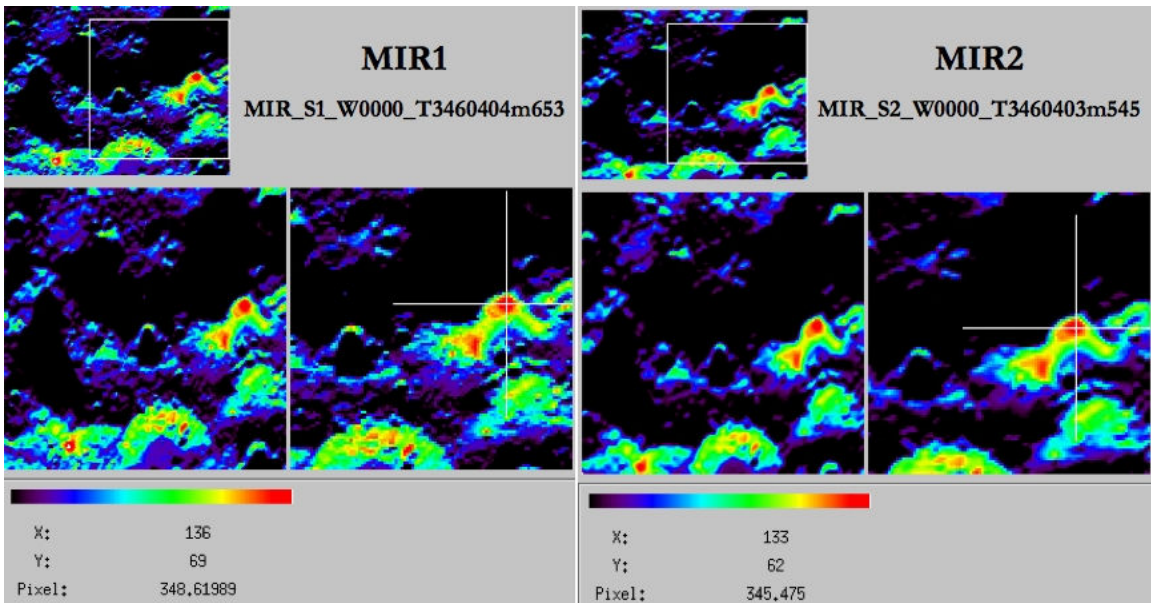


**Figure 14. MIR observed temperatures at impact. The scale is linear with black < 220K, and red mapped to 350 K for both cameras.**
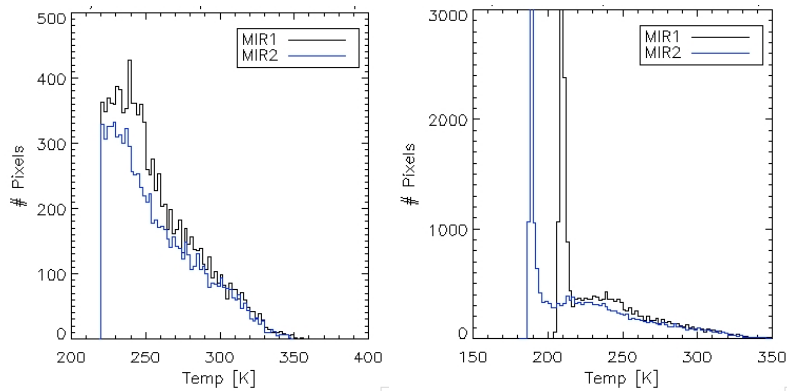


**Figure 15. Temperature ranges in the impact images. (left) Only > 220K data is shown. (right) Data > 125 K is shown. Here the dark cold basins, the source of the large peak, average to 210 K and 190 K for MIR1 & MIR2, respectively.**

To relate DN to temperature [degree K], the following algorithm was used. For degrees C, subtract 273.15 from the calculated degrees Kelvin. The algorithm does not identify pixels that are near the camera's low temperature sensitivity limit. Any temperatures < 220 K will have errors > 30K from this approach.

For MIR1:

1. Apply the DN to temperature polynomial for the MIR1 "Extended Fit" from **Table 3**.

For MIR2:

1. Subtract a global offset calculated from inputting the number of seconds since instrument power on using the polynomial in **Table 4** from the entire DN image.
2. Apply the DN to temperature polynomial for the MIR2 "Extended Fit" from **Table 3**.

# 6   VSP Calibration

VSP integration times can range from 8 ms to 65,535 ms. The VSP has two data-taking modes: single and bracket. Single spectra means a single spectrum of a given integration time is taken per exposure command. Bracket spectra means a "triplet" of spectra in the order "$t$, $t/f$, $t*f$" is taken of the scene per exposure command, where $t$=base integration time and $f$=scalar factor. For example, a bracket spectra with settings $t$=500 ms with $f$=5, will command the VSP to provide a 500 ms, then a 100 ms, and a 2500 ms exposure sequentially. Typical VSP integration times used for LCROSS flight sequences were 100, 200, 400, 500, 2000, and 2500 ms.

The actual spectrum recorded within the VSP is 20 [rows/spatially] x 1044 [columns/spectrally], these 20 rows are co-added internal to the instrument before delivery to the DHU. There is no active cosmic ray removal algorithm used.

Each UV-visible spectrometer (VSP) spectrum has 1044 pixels of information, but only 1024 of the pixels contain spectral information. The mapping of the pixels, adopting the numbering [0:1043] is summarized in Table 5. There are 7 blue bevel, 6 red bevel, 4 red dark, and 3 blue dark calibration pixels. The 'bevel' pixels are sensitive to light, but they are outside of the optical path. The 'dark/blank' pixels are those that are blocked from any light and represent the thermal current background. The red and blue represent the long vs. short wavelength end of the measured spectrum, respectively. For the LCROSS spectrometers, there are 20 'extra' pixels that consist of 7 blue and 6 red bevel pixels, and 3 blue & 4 red dark/blank pixels. Of the four red dark pixels, pixels [1031-1034], pixels 1033 & 1034 are always high, and are flagged as bad. Therefore the 'good' dark reference pixels from the VSP are 1031, 1032, and 1035, 1036 and 1037.

Spectral resolution was measured in the lab using arc lines. The average line FWHM ranged from 1.03 nm (from 300-400 nm), 0.98 nm (from 400-500 nm), and 0.66 nm (from 500-600 nm).

| Table 5. Mapping of VSP pixels to description. | |
|---|---|
| Pixel | Description |
| 0 | Blue Bevel |
| 1 | Spectral Pixel 0 |
| 2 | Spectral Pixel 1 |
| … | …Spectral Pixels… |
| 1023 | Spectral Pixel 1022 |
| 1024 | Spectral Pixel 1023 |
| 1025-1030 | Red Bevel |
| 1031-1034 | Red Dark/Blank |
| 1035-1037 | Blue Dark/Blank |

On-orbit wavelength calibration was performed using high signal-to-noise reflectance spectra from the lunar surface obtained during lunar swingby on DOY09-174. This spectrum is dominated by over 150 strong solar lines (Figure 16). Fifty-one of the strongest absorption lines, excluding blends (e.g., some of the brightest Fraunhofer lines and other FeI lines that spanned over several pixels) were identified and assigned wavelengths (in vacuum) from the NIST Atomic Spectral database (http://physics.nist.gov/PhysRefData/ASD/index.html). Each line's center location (in pixels) was found by subtracting off the continuum and fitting a Gaussian function to identify the peak location to the nearest half-pixel. A 3rd order polynomial fit was fit to map the pixel to wavelength relationship. For these 51 lines, the mapping was found to better than 0.5 nm. In theory, a polynomial fit is not optimal for a grating response function, but this approach was sufficient for the current purpose. A comparison of the wavelength calibrated lunar swingby VSP spectra to the E-490, zero-airmass standard (http://rredc.nrel.gov/solar/spectra/am0/) validated this approach (see Figure 16), identifying most of the solar lines to within 1 nm. The VSP post-flight wavelength calibration is summarized in Table 6. In this numbering scheme, the first and last spectral pixels, pixels [1] and [1024], have wavelengths 262.984 nm 650.300 nm, respectively. Pixel [0] (blue bevel) has wavelength 262.585 nm.

| Table 6. Flight VSP wavelength calibration |
|---|
| $l[nm]= a_0 + a_1x + a_2x^2 + a_3x^3$;  $x = pixel\ number\ from\ [0:1024]$; True spectral pixels are [1:1024], Pixels 0, 1025:1043 have no relevant wavelength calibration |
| $a_0$ = 262.5849218; $a_1$ = 0.398783441; $a_2$ = -1.77053E-05; $a_3$ = -1.93115E-09 |

The flight (FLT) LCROSS UV-visible spectrometer (VSP) was not calibrated with a standard radiance source. An engineering test unit (ETU) underwent two separate types of radiometric calibration: (1) a NIST-calibrated Sphere at NASA Ames in June 2007 (valid for 380-650 nm only) and (2) two NIST-calibrated light sources by the VSP vendor in November 2009. The FLT and ETU units underwent a relative calibration using a smaller integrating sphere to provide a translation from the NIST-calibrated ETU data to the FLT unit in July 2007 for wavelengths 380-650 nm. As the FLT and ETU spectrometers were sensitive from ~250-650 nm, a best-effort radiance calibration for 250-380 nm was calculated by normalizing the vendor provided calibration for the ETU <380 nm, applying a

FLT to ETU response model (extrapolation <380 nm) and normalized to the ARC NIST Sphere calibration at 380nm. The shape and values of the DN to Radiance function used for VSP radiance calibration (PDS 2010-03-17) are shown in **Figure 17**.
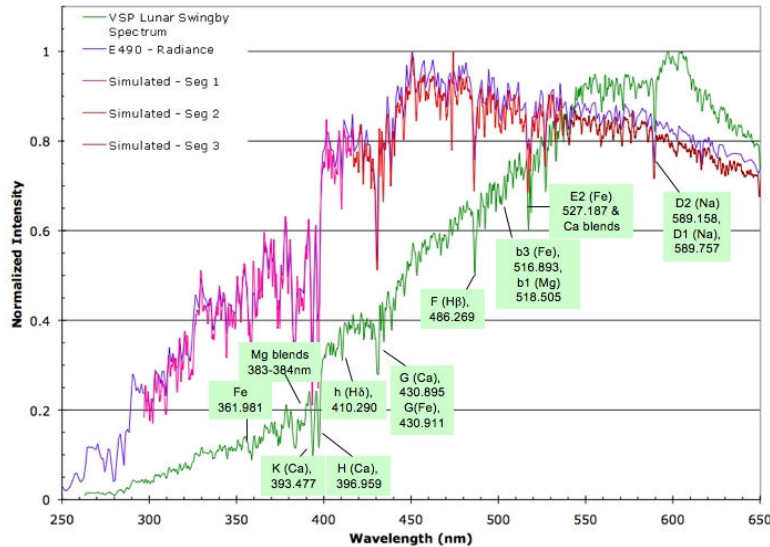


**Figure 16. VSP Flight spectrum (green) compared with solar standard (blue) and some simulated test spectra. The strongest lines are identified. Fifty-one solar lines were used for the wavelength calibration.**

Each VSP pixel is 16-bit, DN=0-65535. 65535 DN is saturation. A flag is identified in the PDS header if there are any pixels from the raw VSP data that are saturated, but no correction for saturation is provided.

The following algorithm was used to calibrate VSP raw data [pixel, DN] to calibrated wavelength and radiance [nm, $W/(m^2 \, \mu m \, sr)$].

1. Apply the wavelength calibration polynomial to the pixels [0:1024] as defined in **Table 6**.
2. For each spectrum of given exposure time subtract a dark value of the same exposure time. This is the mean value from pixels 1031, 1032, and 1035, 1036 and 1037 obtained the same time as the spectrum. This is not a pixel-dependent dark subtraction. This step could be replaced with a pixel-by-pixel dark subtraction, making sure the dark spectra is of the same exposure time as the signal spectrum. To first order, the VSP dark spectra (with the TEC enabled to -10 °C) have 2360 DN raw counts for integration times < 1 s. For integration times ≥ 2.5 s, dark spectra have ~2370 DN.
3. Time-normalize the spectra by taking (Spec-Dark)([DN] and dividing by the integration time in seconds, to get a [DN/s].
4. Divide this time-normalized spectra by the DN/Radiance Conversion [$DN/(W/m^2 \, \mu m \, sr)$] **Figure 17**.
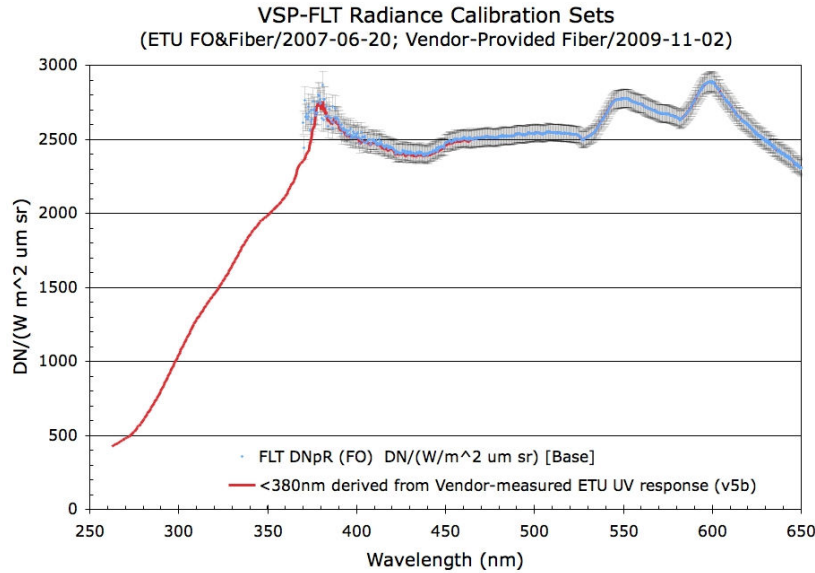
**Figure 17. Derived VSP-FLT NIST Sphere radiance calibration (380-650nm) and vendor-provided UV calibration normalized to match at 380 nm.**

VSP radiance calibration was performed on Earth calibration data and compared with a mid-latitude summer, uniform albedo SBDART model. Two 250-380 nm calibration methods (v3a/grating; v5b/vendor scaling) to Earth spectra from DOY09-213 are shown in Figure 18. 10% error bars on the SBDART model are indicated. The SBDART model did not take into account the actual cloud cover or illumination of the actual data set. The computed radiances for wavelengths longward of 345 nm are within 10% of this particular Earth reflectance model. The VSP lunar radiance at the time of impact was also computed and matched lunar reflectance models to 10-15% at all wavelengths. The v5b/vendor scaling model was used for the 2010-03-17 PDS delivery.
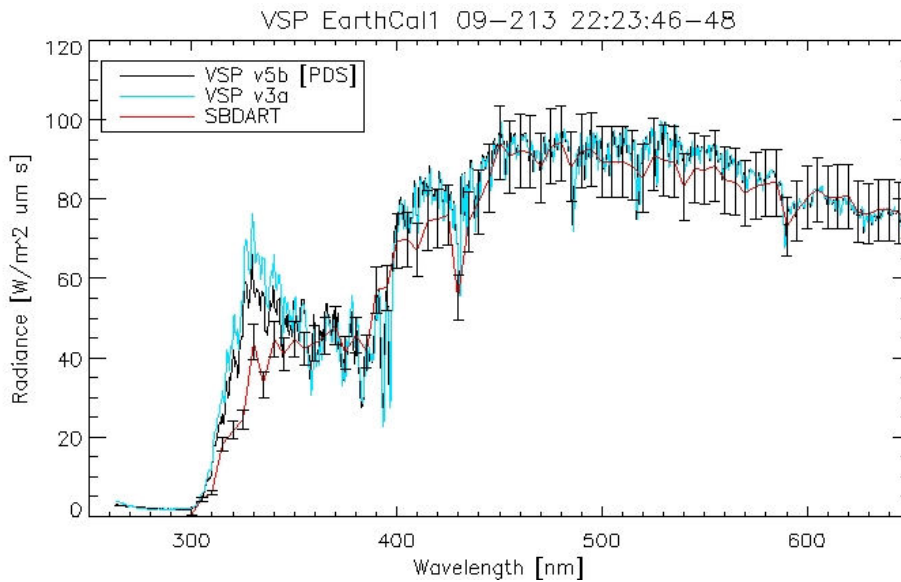


**Figure 18. Earth spectra from DOY09-213 taken with VSP calibrated with the two <380 nm methods described and compared to mid-latitude summer SBDART Model. The 2010-03-17 PDS release uses v5b (black line).**

# 7 NSP1 Calibration

The near infrared spectrometers have three modes: Hadamard (or full spectrum), Flash (5 spectral masks plus one dark mask), and Diagnostic. Hadamard and Flash modes were both used in NSP1 flight data.

The NSP1 Hadamard mode provides spectral samples from 1.16932 to 2.47862 μm in 100 pixel elements. Spectral calibration was performed pre-flight using a calibrated monochromator with a 1 nm wide slit that stepped at 0.01 μm increments across the NSP1 wavelength range. Hadamard spectra were taken at each setting. Each Hadamard transform of the monochromator's 1 nm-wide line extended across several pixels. A Gaussian was fit to derive the center position (fractional pixel) of the profile. The results of a 3rd order polynomial fitted to wavelength (from the monochromator) versus pixel-fraction (Gaussian-fitted) to derive the wavelength calibration are summarized in Table 7. During this test, the NSP1's line profile FWHM was also measured. Fully resolved instrument profiles at 1.4803 and 2.0644 μm have FWHM = 0.0341 and 0.0362 μm, respectively.

| Table 7. Flight NSP1 wavelength calibration HADAMARD mode |
| --- |
| $l[mm] = a_0 + a_1x + a_2x^2 + a_3x^3;\ x = pixel\ number\ from\ [0:99]$ |
| $a_0 = 1.1693218;\ a_1 = 0.013657562;\ a_2 = -1.0213915e\text{-}06;\ a_3 = -3.3793280e\text{-}08$ |

Mask (flash) mode provides six spectral samples whose spectral properties are summarized in Table 8. These parameters were derived using the same stepped monochromator approach as for Hadamard mode. Mask 1 is a 'dark mask' where the MEMS mirrors are positioned not to reflect light into the spectrometer. This dark mask value is subtracted from each of the five spectral masks on a per scan basis to remove drifts in the dark curent. The parameter definitions for the masks are shown in Figure 19. The normalized NSP1 mask profiles measured are shown in Figure 20.

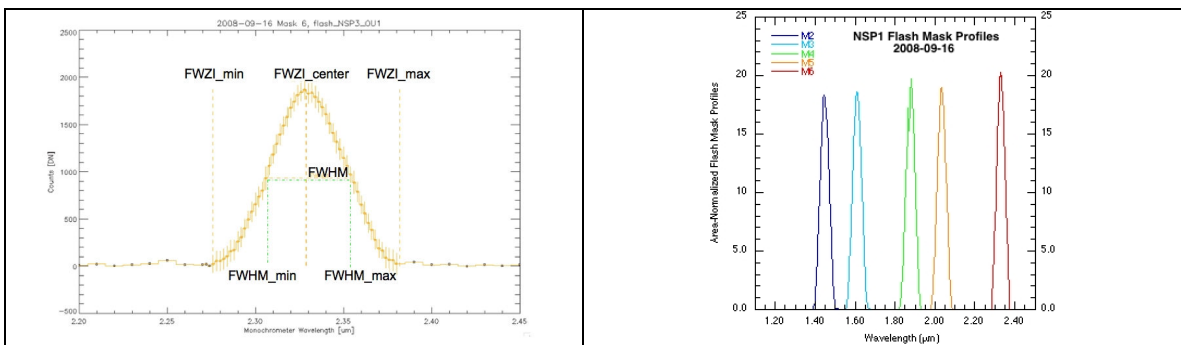| Table 8. Flight NSP1 wavelength calibration FLASH mode | | | | | | |
| --- | --- | --- | --- | --- | --- | --- |
| Mask | FWZI_center μm | FWZI min μm | FWZI max μm | FWHM_center μm | FWHM min μm | FWHM max μm |
| M1 | Dark Mask; All MEMS mirrors 'Off' | | | | | |
| M2 | 1.448 | 1.394 | 1.502 | 1.447 | 1.420 | 1.474 |
| M3 | 1.610 | 1.556 | 1.664 | 1.610 | 1.584 | 1.636 |
| M4 | 1.877 | 1.824 | 1.930 | 1.877 | 1.852 | 1.902 |
| M5 | 2.032 | 1.978 | 2.086 | 2.034 | 2.008 | 2.060 |
| M6 | 2.332 | 2.276 | 2.382 | 2.331 | 2.308 | 2.354 |

| Figure 19. Mask profile parameters description. | Figure 20. Normalized NSP1 flash mask profiles. |
|---|---|

Earth spectra were obtained three times during the LCROSS mission. Application of the above described NSP1 wavelength & post-flight calibration (see below) to the flight data for EarthCal1/DOY09-213 (black dots) compared with a SBDART model of the Earth's atmosphere for mid-latitude summer, uniform albedo (blue dots) confirms good matching spectrally to Earth's atmospheric features, mainly $H_2O$ and $CO_2$ at this low (R~20-60) resolution (Figure 21).
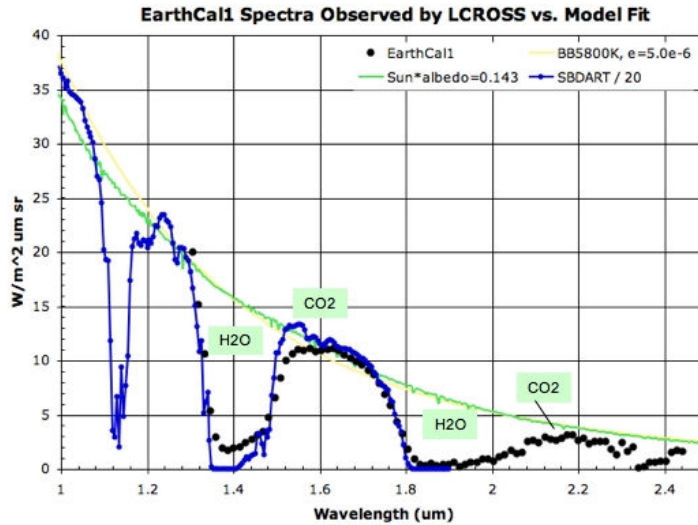


**Figure 21. NSP1 Earth Cal 1 data (black dots) compared with various models for Earth's spectrum (green, yellow, blue dots/line).**

Radiance calibration for the NSP1 (both Hadamard and Flash mode) was performed using the NIST calibrated sphere at NASA Ames Airborne Sensor Lab in September 2009. To assess the quality of the systematic errors in the use of the ARC Calibration Lab NIST Sphere, a detailed study was performed on the NSPs, where the location of the fore-optics to sphere center was adjusted by a few inches vertically and horizontally, different test fibers were used, test fibers were bent with one and two bends, and various baffling schemes were introduced. Assuming the sphere remained constant, as it should have, variances in the detected signal could be computed. Systematics introduced at most ~4% error.

It was observed early in the mission, during lunar swingby (DOY09-174), that applying the September 2008 lab-based radiometric calibration relationships for the two near infrared spectrometers introduced "water" in the spectra. It was quickly realized that the lab-based radiance calibration provided a 1 meter long path length that introduced water absorption that was not fully accounted for by the NIST radiance curve (20080314105200Archi.txt). Solar spectra observed by NSP2, on the final day of the mission (DOY09-282), after 112 days in space, when it was assumed all water in the solar view diffuser and 145 cm fiber was baked off, was used to correct the water profiles in the lab-based NIST calibration radiance used for NSP1 radiance calibration. Figure 22 compares the original NIST sphere radiance (black) against the derived 'water-adjusted' NIST sphere radiance (blue) that represents the proper water contamination from the NIST sphere. The 'water-adjusted' NIST sphere radiance was used for the radiance calibration of NSP1 for both Hadamard and Mask mode. For the Flash mode, the 'water-adjusted' NIST sphere radiance is convolved with the

derived instrument profile for each mask to provide an in-band radiance value (**Figure 23**). The resulting DN per Radiance (DNpR or [DN/(W/m2 μm sr)]) for Hadamard and Flash mode computed for the flight NSP1 Hadamard mode is shown in **Figure 24** and **Figure 25**, respectively. The error bars are dominated by uncertainties in the NIST Radiance (20080314105200Archi.txt) of the Lab Sphere.

The following algorithm was used to calibrate NSP raw data [pixel, DN] to calibrated wavelength and radiance [μm, W/(m² μm sr)].

NSP1 Hadamard:
  1. Apply the wavelength calibration polynomial to the pixels [0:99] as defined in **Table 7**.
  2. Divide the Hadamard transformed spectrum [DN] by the DN/Radiance conversion [DN/(W/m^2 μm sr)] shown in **Figure 24**.

NSP1 Flash:
  1. Apply the wavelength calibration values for the FWZI center in microns to each of the masks as defined in **Table 8**.
  2. Subtract the first mask/M1 (dark mask) from each of Mask 2, 3, 4, 5, and 6 taken from the same scan.
  3. Divide each dark subtracted mask by the DN/Radiance conversion [DN/(W/m^2 μm sr)] as shown in **Figure 25**.
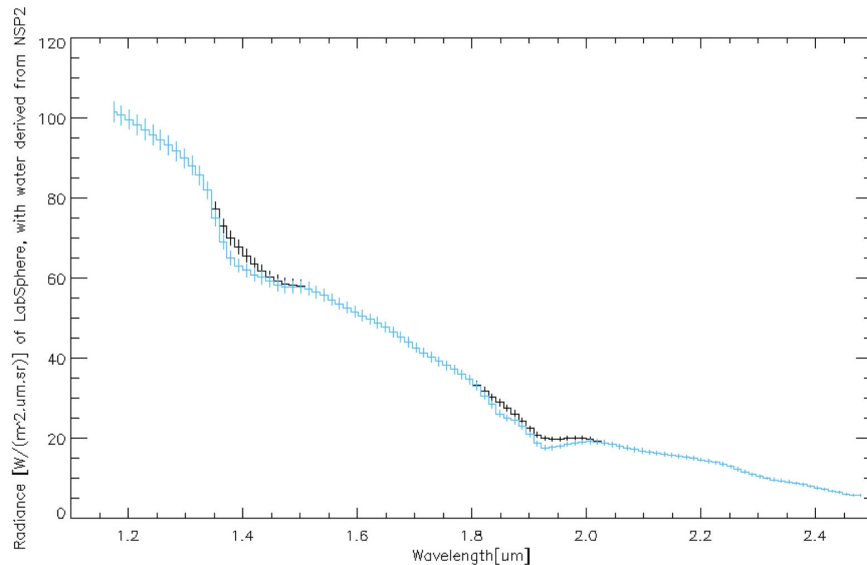


**Figure 22. NSP2-CORRECTED-to-NSP1-OPTICS-WATER-CORRECTED derivation of NIST Sphere Radiance (light blue) plotted on top of the original NIST Sphere Radiance (black, 20080314105200Archi.txt)(20080314105200Archi.txt), showing there were deeper water bands in the NIST Sphere that need to be accounted for in the NSP1 radiance calibration using the NIST sphere.**
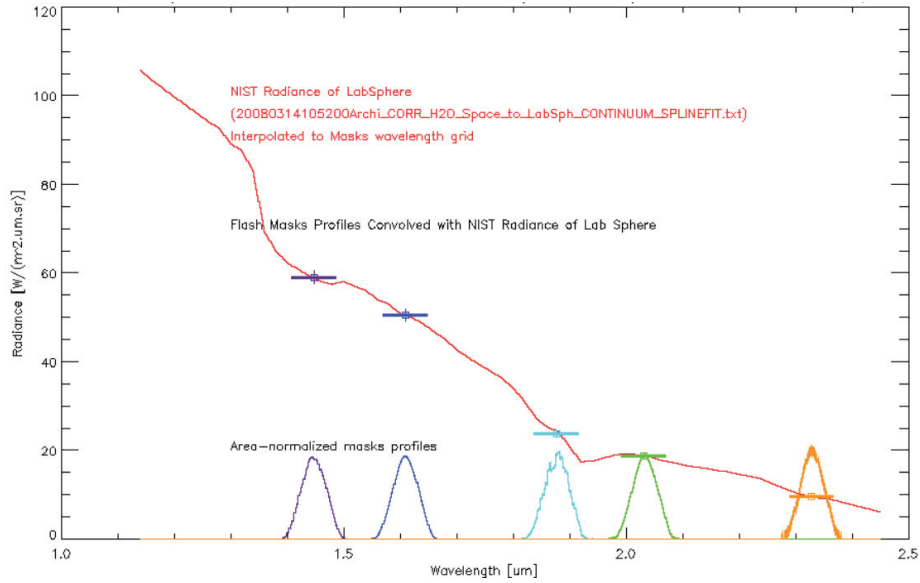
**Figure 23. Radiance values of the convolved mask profiles of the 'water-adjusted' NIST sphere radiance for NSP1. The area-normalized mask profiles are superimposed to illustrate the wavelength range over which the sphere's radiance is integrated.**
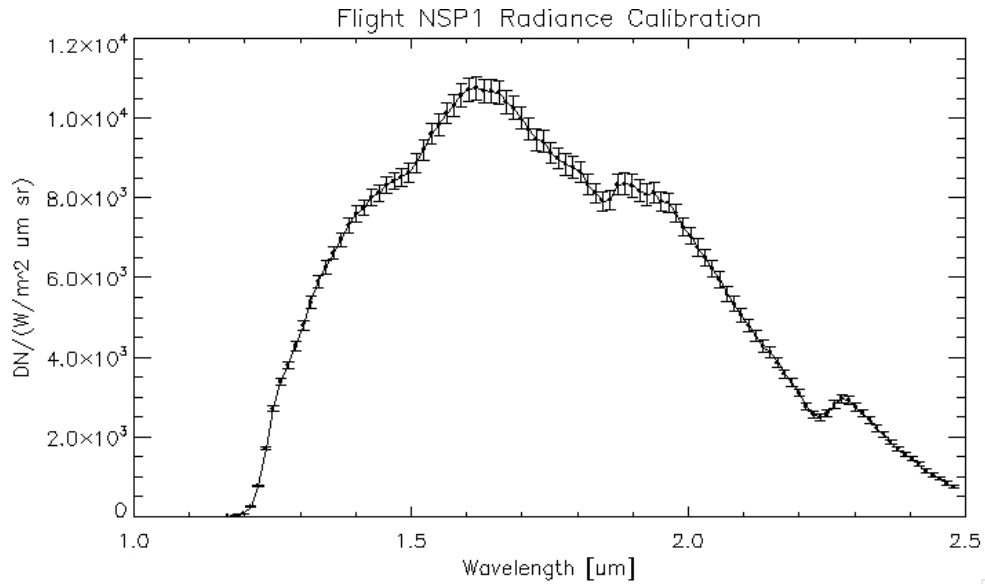


**Figure 24. NSP1 Hadamard radiance calibration for the flight data sets.**
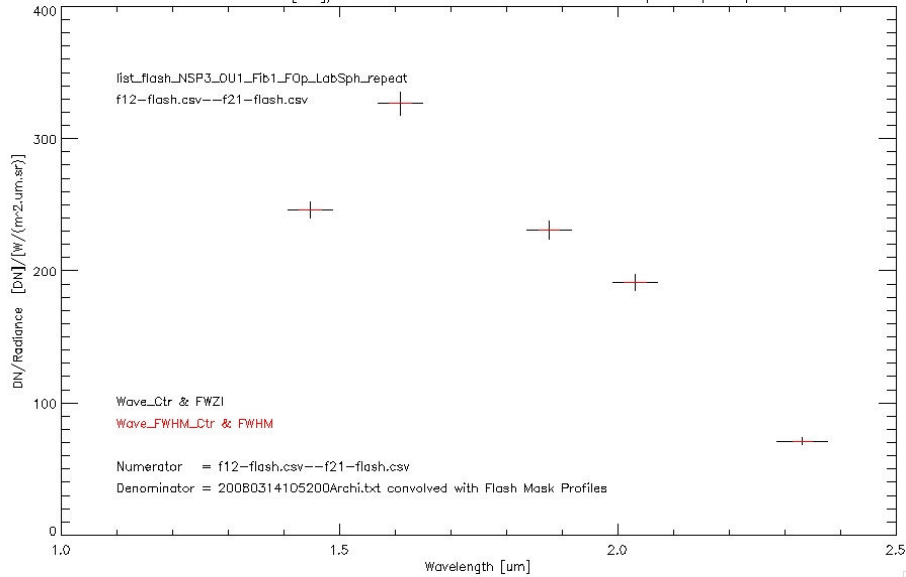
**Figure 25. NSP1 flash radiance calibration for the flight data sets.**

# 8   NSP2 Calibration

Hadamard mode was the primary mode for NSP2 flight data. NSP2 was operated briefly in flash, but only during finite times during calibration activities and always at low Sun angle (no signal). There are no calibrated products delivered to the PDS 2010-03-17 for NSP2 in flash mode.

The NSP2 Hadamard mode provides spectral samples from 1.17464 to 2.47925 μm in 100 pixel elements. Spectral calibration was performed pre-flight using a calibrated monochromator with a 1 nm wide slit that stepped at 0.01 μm increments across the NSP1 wavelength range. Hadamard spectra were taken at each setting. Each Hadamard transform of the monochromator's 1 nm-wide line extended across several pixels. A Gaussian was fit to derive the center position (fractional pixel) of the profile. The results of a 3$^{rd}$ order polynomial fitted to wavelength (from the monochromator) versus pixel-fraction (Gaussian-fitted) to derive the wavelength calibration are summarized in Table 9. During this test, the NSP1's line profile FWHM was also measured. Fully resolved instrument profiles at 1.3785 and 2.0724 μm have FWHM = 0.0330 and 0.0316 μm, respectively.

| Table 9. Flight NSP2 wavelength calibration HADAMARD mode |
|---|
| *l[mm]= a$_0$ + a$_1$x + a$_2$x$^2$ + a$_3$x$^3$;  x = pixel number from [0:99]* |
| $a_0$ = 1.1746421; $a_1$ =0.013720972; $a_2$ = -4.0204582e-06; $a_3$ = -1.4801439e-08 |

Radiance calibration for the NSP2 (Hadamard mode) was derived using the standard solar spectrum (E490_00a_AM0.xls, http://rredc.nrel.gov/solar/spectra/am0/ASTM2000.html) and corrected for cosine angle to the Sun at the time the data was taken. NSP2 observed the Sun in different sequences for a range of angles. The solar spectrum used for the flight calibration was taken on the last day of the mission, DOY09-282, when after 112 days in space it was assumed any water or other contaminants in the diffuser and fiber options were baked out. A careful look was performed to rule out contamination by hydrazine, the propellant used for attitude control during instrument operations, and ammonia, its primary

decay product. The data set during the final hour had a 15.3° angle to the Sun. The resulting DNpR radiance calibration function for Hadamard mode computed for the flight NSP1 Hadamard mode is shown in **Figure 26**. As NSP2 observed the Sun, on a trajectory that tracked the Sun, the error bars shown here are small due to the strong signal (millions of counts) and a steady source.

The following algorithm was used to calibrate NSP2 raw data [pixel, DN] to calibrated wavelength and radiance [$\mu$m, $W/(m^2 \mu m\ sr)$].

NSP2 Hadamard:
1. Apply the wavelength calibration polynomial to the pixels [0:99] as defined in **Table 9**.
2. Divide the Hadamard transformed spectrum [DN] by the DN/Radiance conversion [DN/(W/m^2 $\mu$m sr)], which is shown in **Figure 26**.
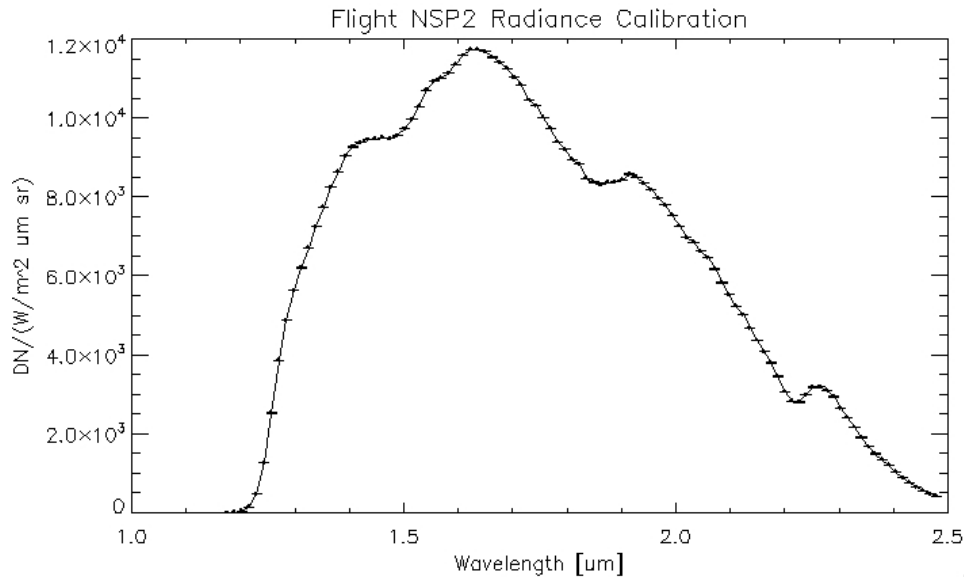


**Figure 26. NSP2 Hadamard radiance calibration for the flight data sets.**

# 9   TLP Calibration

This section describes the calibration performed for the TLP_CAL_DS dataset. This calibration mapped raw data number to detector voltage after correcting for detector temperature variation. The voltage was normalized to 0°C. Mapping from this voltage to radiance required the detector response function at 0°C and a model of the input spectrum, i.e., the flash spectrum in this case. Because a model was required to go further, only the temperature-normalized detector voltage was provided.

The steps to convert raw data numbers to temperature-normalized voltage were:

1. Convert the raw temperature sensor data number to a voltage
2. Convert the temperature sensor voltage to a temperature
3. Convert the raw data number to an un-normalized voltage

4.  Convert the un-normalized voltage to a temperature-normalized voltage

The following sections detail these steps.

### 9.1  Convert the raw temperature sensor data number to a voltage

The TLP had two internal temperature sensors, ADP1 and ADP2. Sensor ADP1 was attached the TLP detector housing, so it was used for this calculation. ADP2 used an equivalent equation with the same linear coefficients.

ADP_1_Voltage = a * DN + b

Where DN is the raw, int16 data number for ADP_1,
a = 0.0003051758, and b = 0.000

### 9.2  Convert the temperature sensor voltage to a temperature

Temperature sensor voltage was converted to temperature as follows. Equations for both sensors are shown:

$$T1_{CORRECTED} = 1.0065 \cdot (100 \cdot ADP\_1\_Voltage - 273.15) - 0.8879 \text{, deg C}$$

$$T2_{CORRECTED} = 1.0044 \cdot (100 \cdot ADP\_2\_Voltage - 273.15) - 0.5473 \text{, deg C}$$

Where:

$T1_{CORRECTED}$ was the corrected temperature converted from V1

$T2_{CORRECTED}$ was the corrected temperature converted from V2

$ADP\_1\_Voltage$ was the voltage output from channel 1 (ADP_1)

$ADP\_2\_Voltage$ was the voltage output from channel 2 (ADP_2)

ADP_1 was used for all calibrated TLP data in the PDS release.

### 9.3  Convert the raw detector data number to an un-normalized voltage

The TLP detector raw data numbers were converted to un-normalized voltage using the same equation as the temperature sensors:

$V_a$ = a * DN + b

Where DN was the raw, int16 data number from the photometer,
a = 0.0003051758, and b = 0.000

### 9.4  Convert the un-normalized voltage to a temperature-normalized voltage

Rename $T1_{CORRECTED}$ to $T_a$:

$$T1_{CORRECTED} = T_a$$

The measured voltage, $V_a$, and measured temperature, $T_a$ were converted to temperature-normalized voltage $V_b$ at temperature $T_b$ as follows:

$$V_b = V_a \cdot \left( \frac{a' \cdot T_b^2 + b' \cdot T_b + c'}{a' \cdot T_a^2 + b' \cdot T_a + c'} \right), \text{ volts}$$

Where:

$V_a$ = voltage measured at temperature $T_a$

$V_b$ = voltage expected at temperature $T_b$

$T_a$ = temperature at which voltage measurement is made

$T_b$ = temperature at which you want to convert the voltage read

$a' = 3.453174\text{E-}04$

$b' = \text{-}3.10608\text{E-}02$

$c' = 1.0000$

0°C was chosen as the reference temperature. The voltage appearing in the calibrated TLP data products is $V_b$ calculated for $T_b = 0°C$, $T_a = T1_{CORRECTED}$, and $V_a$ was computed as described in section 9.3.

## *9.5* TLP Thermal & Optical Calibration

A thermal-optical calibration test was performed in June 2007. This test measured the TLP SEM response at steady-state temperatures over the temperature range of 0°C to +40°C at 5°C intervals for varying signal and background amplitudes at each temperature state. The light sources, kept at room temperature outside the thermal chamber, were (1) a bright white LED for the flash spectrum, and (2) an incandescent lamp source located behind a translucent white sheet to provide a continuum for a simulated lunar background (nulled out by the high-pass filter). Knowledge of the light sources' incident irradiance was performed by replacing the TLP/SEM with a calibrated Newport power meter (Newport Model #1815-C, Sensor Head #818-SL) and a matching SEM lens. This test provided the conversion between measured "TLP/SEM Voltage" to "Irradiance in nW/cm$^2$" for a variety of SEM temperatures.

The TLP responsivity at discrete optical wavelengths in the 400 nm to 1000 nm band was next measured at room temperature in July 2007. Here, the test used a calibrated monochromator with the addition of two external mirrors and one lens to collimate the exit light and fill the full FOV of the TLP optics. The same calibrated Newport sensor was used to provide indication of power/area (nW/cm$^2$) during the measurement. The TLP's response was measured at 400, 450, 500, 543.5, 632.8, 700, 750, 800, 861, 900, 950 and 1000 nm.

Combining the manufacturer specification and the thermal response data from the thermal optical test described above, the TLP responsivity vs. wavelength at 0°C was determined. A family of curves describing the TLP responsivity vs. wavelength at other operational temperature ranges was also calculated (Figure 27).

A 4th order polynomial was fitted to the TLP response data points acquired from the monochromator calibration. This equation calculates the TLP sensitivity at 0°C:

$$R_{0\deg C} = a' \cdot \lambda^4 + b' \cdot \lambda^3 + c' \cdot \lambda^2 + d' \cdot \lambda + e', \quad (\text{V/nW/nm})$$

Where:

$R_{0\deg C} = \text{TLP Responsivity at } 0°C$

$\lambda = \text{wavelength in nm, from 400 to 1000 nm}$

$a' = 1.433843E\text{-}10$

$b' = -4.343039E\text{-}07$

$c' = 4.517304E\text{-}04$

$d' = -1.874399E\text{-}01$

$e' = 2.726991E\text{+}01$

This equation is the most directly useful one with the calibrated TLP data product.

This equation calculates the responsivity at temperature, $T_a$, given the responsivity at 0°C:

$$R_{@T_a} = R_{0\deg C} \cdot \left( a' \cdot T_a^2 + b' T_a + c' \right), \quad \text{V/nW/nm}$$

Where:

$R_{@T_a} = \text{TLP Responsivity at } T_a$

$R_{0\deg C} = \text{TLP Responsivity at } 0°C \text{ computed from above}$

$T_a = \text{Temperature at which Responsivity is to be obtained}$

$a' = 3.453174E\text{-}04$
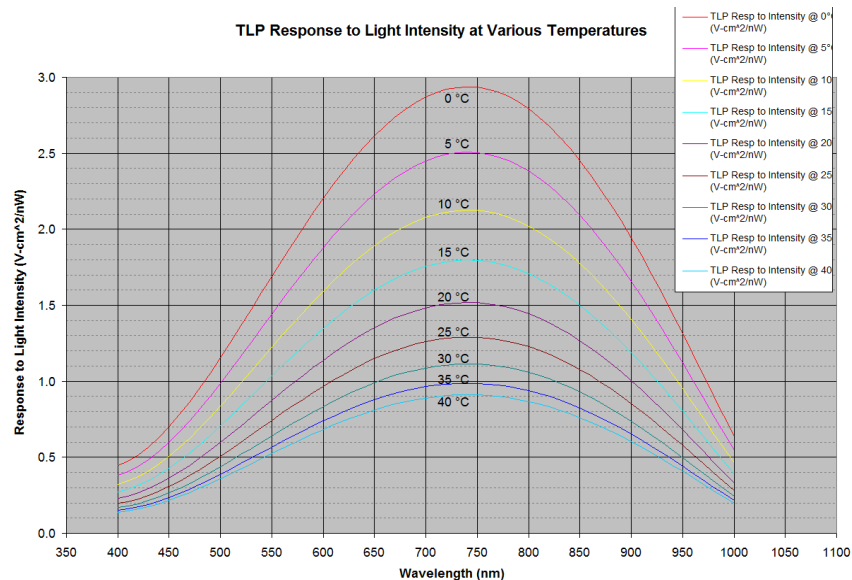
$b' = -3.10608E\text{-}02$

$c' = 1.00000$



**Figure 27. TLP spectral response function for a range of sensor temperatures.**

The TLP response at room temperature and at 0°C was compared to the manufacturer's spectral sensitivity curve to show how close the measured TLP response matched the manufacturer's data (**Figure 28**).
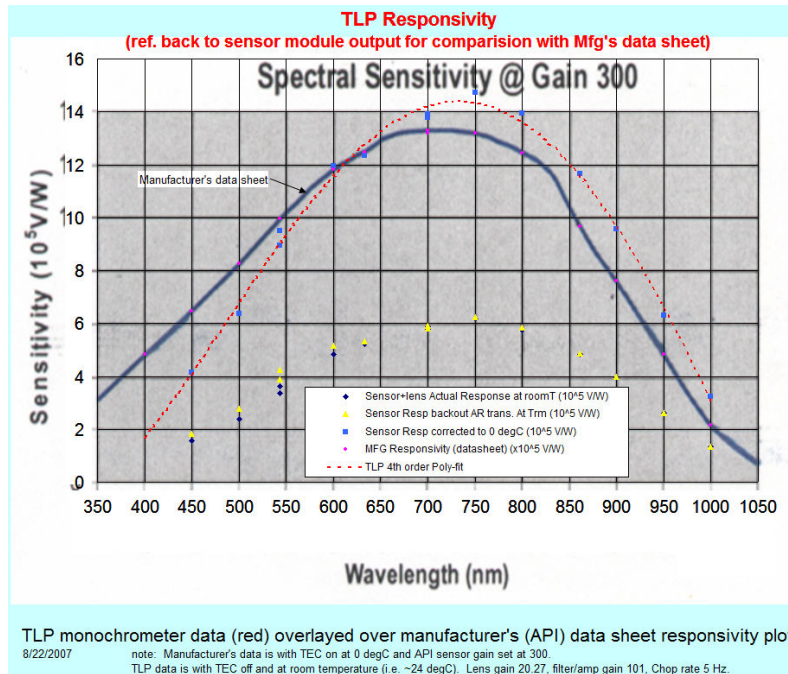
**Figure 28. TLP sensor measured response (red curve) compared with manufacturer's data (blue curve).**

# 10 DHU Time Calibration

This section describes the process of assigning UTC timestamps to all LCROSS data products delivered to the Planetary Data System.

## 10.1 Relevant Clocks

Including Coordinated Universal Time (UTC), five clocks were involved in assigning timestamps to LCROSS data products. These clocks were:

1. The spacecraft Command & Data Handling (CDH) system clock
2. The Data Handling Unit (DHU) Video Control Board (VCB) clock
3. The DHU Serial Digital Board #1 (SDB1) clock
4. The DHU Serial Digital Board #2 (SDB2) clock
5. The Visible and Ultraviolet light Spectrometer (VSP) clock
6. True UTC

The clocks were used to timestamp data products as follows:

1. The VCB clock was used to timestamp images captured by the VIS, NIR1 and NIR2 cameras.
2. The SDB1 clock was used to timestamp images captured by MIR1 and spectra captured by the NSP1 and VSP.
3. The SDB2 clock was used to timestamp images captured by MIR2, spectra captured by NSP2 and data captured by TLP.

## 10.2 Summary of Clock Offsets

Offsets between all clocks were derived for the PREIMPACT and IMPACT data collection periods and between some clocks during other periods as required for instrument calibration.

Offsets for PREIMPACT and IMPACT:

> At Centaur impact and at SSC impact (units are seconds):
>
> > VCB = UTC + 0.077
> > SDB1 - 1 = VCB
> > DB2 - 1 = VCB
>
> > These offsets were stable during the interval between Centaur impact and SSC impact. There were 1 second jumps during the PREIMPACT data collection phase (described below).
>
> > These offsets have been applied to all PREIMPACT and IMPACT data products such that their timestamps reflect our current estimate of true UTC time. Timestamps were applied to VSP spectra using more steps as described below.

Offsets for SWINGBY:

> > VCB = UTC + 1.533535
> > SDB1 = VCB - 2
>
> > These offsets were used for payload boresight measurements but not applied to the SWINGBY data products. Timestamps for those products reflect the clock on the circuit board that generated the downlink packet (described below).

## 10.3 Summary of Data Flow and Time Distribution

Each of these clocks was implemented on a distinct digital circuit board, and time information was distributed to keep them synchronized. Figure 29 shows how time information was distributed, starting in LCROSS mission control (top right) and ending at the data handling circuit boards onboard the spacecraft (lower left). All the boxes in this diagram are part of the LCROSS payload except the CDH and ground system, which is on the spacecraft and ground, respectively.

The VSP clock was the only exception: it was free running and not synchronized to any other clock, although, as described later, it was used to assign times to some VSP data products.

CDH is the root of the clock distribution graph onboard the spacecraft. CDH generated an accurate, once-per-second clock pulse followed by a time-at-the-tone message giving the date and time of the most recent pulse. The pulse was distributed to all three payload data handling circuit boards in parallel and none of the instruments. The time-at-the-tone

message was distributed to the VCB and from there, to SDB1 and SDB2. The message was not changed as it passed through VCB.
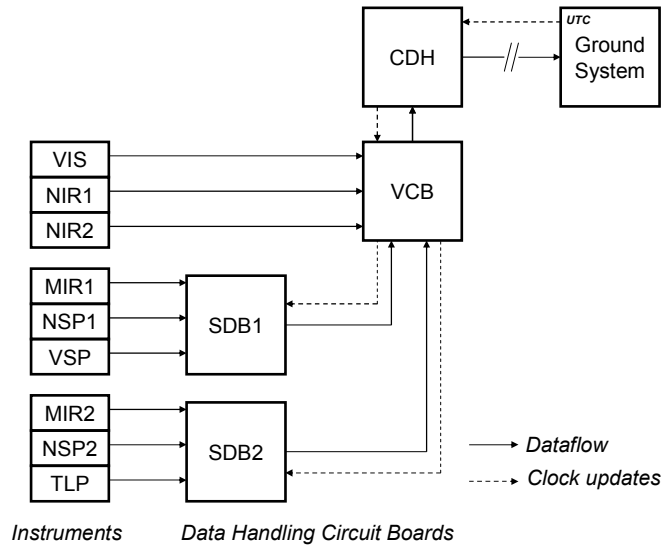


**Figure 29. Time stamp data flow.**

## 10.4 Time Synchronization Error Sources

Several sources of error had to be corrected to assign accurate times to data products. This correction was done for the data products within the PREIMPACT and IMPACT data collection periods but not for the products in within the other data collection periods. The error sources were:

1. **Spacecraft CDH clock drift**. This error was accounted for in the usual way by measuring the delta between the spacecraft clock (CDH) and the DSN receiving station's clock and accounting for light travel delays. At intervals during the mission, the CDH clock was adjusted to more closely reflect true UTC time. This error was measured and corrected 4 hours before Centaur impact. The drift rate of CDH had been measured earlier in the mission and was applied over the 4 hour interval to calculate the CDH offset at the time of impact.

2. **Intermittent, one second error in time interpretation on VCB, SDB1 and SDB2**. A bug in SDB and VCB software effected interpretation of the time-at-the-tone message. This bug caused the receiving circuit board's interpretation of the clock pulse to include a 1 second error that came and went at intervals of 1 second to several minutes. The error, if present, resulted in the receiving board being exactly 1 second ahead of the intended time. This was the dominant error source. Since its effect was in discrete jumps, it was relatively straightforward to correct.

3. **DHU load**. During the final descent to the moon, processor load on DHU circuit boards was sufficiently high that it delayed timestamping some packets. This occurred during the PREIMPACT period and during the middle of the impact period. It did not occur from one minute before the Centaur impact until 30

seconds afterwards because the DHU was lightly loaded during that period. VSP packets were impacted by this effect, and their timestamps were corrected.

## *10.5* VSP Time Correction

This section applies to timestamps for VSP packets during the PREIMPACT and IMPACT data collection periods.

VSP timestamps are irregular due to high DHU processer loads. To avoid this irregularity, the VSP's internal clock is used as the basis for the calibrated timestamps. The VSP internal clock was stepped down to produce a 1 millisecond counter contained in spectra transmitted from the spectrometer to the DHU. This internal clock was not calibrated prior to launch, nor was it synchronized to any other clock during flight. However, the VSP internal clock's drift relative to the CDH clock was 0.3 sec / hour. After correction of this drift, the VSP internal clock was the basis of the VSP spectra timestamps.

The VSP clock drift relative to CDH was calculated by choosing two bracket-mode spectra taken at times when the DHU was relatively unloaded. These spectra are at timestamps:

    3457427853
    3460405859

These are uncorrected, 'spacecraft' timestamps generated from the SDB2 clock.

The first timestamp corresponds to the first bracket mode spectra taken during PREIMPACT. The second timestamp corresponds to the group of three spectra timed to surround the Centaur impact flash. In both cases, the SDB2 processor was relatively unloaded.

The estimated VSP drift with respect to SDB2 was:

$$\begin{aligned}
\text{drift} \quad &= (VSP\_2 - VSP\_1) \,/\, (SDB2\_2 - SDB2\_1) \\
&= (3007531 - 29268) \,/\, (3460405859 - 3457427853) \\
&= 2978263 \,/\, 2978006 \\
&= 1.000086299356012
\end{aligned}$$

During this period, drift between SDB2 and CDH was modeled as 0 as it was corrected whenever the error reached 1 msec. This correction was done approximately every two minutes during PREIMPACT and IMPACT. The VSP timestamps appear as metadata with each spectra. The timestamps chosen are for S3, the third spectra in each triple. Note that this clock skew gives a deviation of ~0.3 sec over the span of an hour.

This skew value was applied to each spectra's internal VSP-supplied timestamp as:

$$utc\_time\_partial = 3460405859 + (VSP - 3007531) * 1.000086299356012$$

This equation takes the spectra surrounding the Centaur impact as the zero point, subtracting the VSP internal time for the third spectra for that event, applying the skew, then adding the DHU timestamp.

The final equation contains two additional corrections:

UTC = (3460405859-180+(VSP-3007531)*1.000086299356012) -1000 - 78

These three additional corrections, 180 msec, 1000 msec, and 78 msec respectively reflect the time to transmit the spectra from the VSP to the DHU, the delta between SDB2 and CDH and the delta between the spacecraft clock and true UTC after correction 4 hours before Centaur impact. This final equation reflects our best estimate of the end of the integration period for each spectrum.

# Notes on Alpha-Particle X-ray Spectrometer (APXS) Data Reduction

R. Gellert, J. Brückner, G. Dreibus, G. W. Lugmair, R. Rieder, H. Wänke and J. Zipfel,
Max-Planck-Institut für Chemie, Department of Cosmochemistry, Becher-Weg 27, D-55128 Mainz, Germany
J.L. Campbell, J. Maxwell and M. Omand
Department of Physics, University of Guelph, Guelph, Ontario, Canada N1G 2W1

## Introduction

The Alpha-Particle X-ray Spectrometers (APXS) [1] on board of NASA's MER-rovers *Spirit* and *Opportunity* are small instruments, with which the chemical composition of rocks and soil can be measured by simply holding them against a sample for some time (from 10 minutes to several hours - the longer, the more accurate). The instruments have high sensitivity and selectivity for all essential rock-forming elements, because they employ radioactive sources of $^{244}$Cm for excitation, and novel x-ray detectors for registration of the characteristic x-rays, emitted by the atoms in the sample: the sources emit alpha particles and x-rays, thereby effectively exciting light atoms, like Na, Mg, Al, or Si, as well as heavier atoms like Fe, Ni, Zn or Br. These sources have been especially developed for use in the APXS by the Russian Central Research Institute for Atomic Reactors in Dimitrovgrad [2]. They consist of a thin layer of curium-silicide on highly polished semiconductor-grade silicon wafers. The detectors are *silicon drift-chamber* designs, manufactured from high-purity, high-resistivity silicon by modified integrated circuit manufacturing techniques (processing of both sides of a silicon wafer is required), and containing matched first stage preamplifier transistors on the detector chips. This design results in an extremely small effective detector/amplifier-input capacitance. Due to this fact and to very small leakage currents (both bulk and JFET gate) these detectors exhibit excellent low-noise performance at temperatures close to ambient. They are a German development and are commercially available from Ketek GmbH, Munich [3]. It is most unfortunate that this feature could not be fully exploited with the flight instruments in their flight configuration: good resolution could only be obtained at temperatures below -30 °C. To explain the reasons is beyond the scope of this note: suffice it to say that we have only become aware of the circumstances at the time of integration, and that nothing could be done to resolve the problem at this late moment. In the test configuration the flight instruments did indeed deliver spectra with good resolution at temperatures as high as -10 °C and would have been perfectly suitable for *touch-and go* campaigns.

To illustrate the advantages of the *alpha plus x-ray excitation* approach, Fig.1 shows a comparison of spectra, obtained with the same sample (SSK 1.1, an andesite from a South Pacific island, which is similar in composition to the rocks at the Mars-Pathfinder landing site), using (a) combined excitation by alpha particles and x-rays (Pu L-series) from a $^{244}$Cm source, (b) excitation by x-rays from a $^{244}$Cm source only (alpha particles are blocked by a thin aluminium foil), and (c) excitation by a 20 keV electron-beam in a Scanning Electron Microscope.
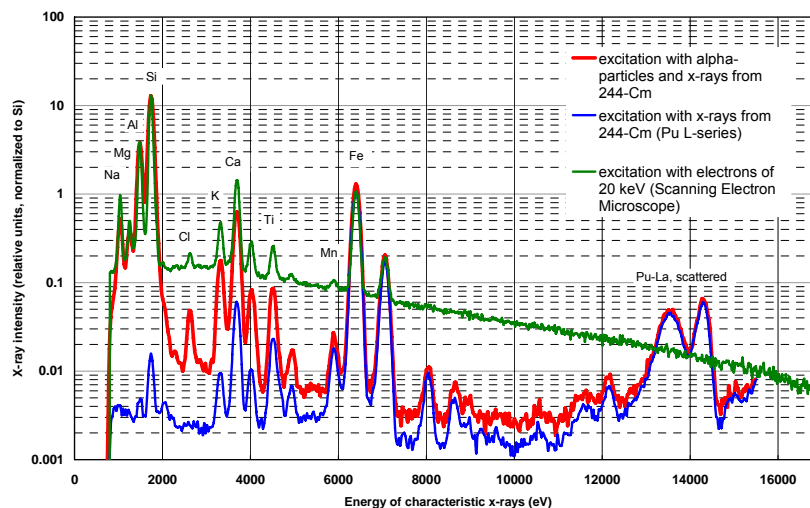


Fig 1: Comparison of x-ray spectra obtained with different excitation sources. Sample: SSK 1.1 (Andesite)

Fig. 2 shows a photograph of the flight sensor, and Fig. 3 shows the location of the APXS on the rover's Instrument Deployment Device.
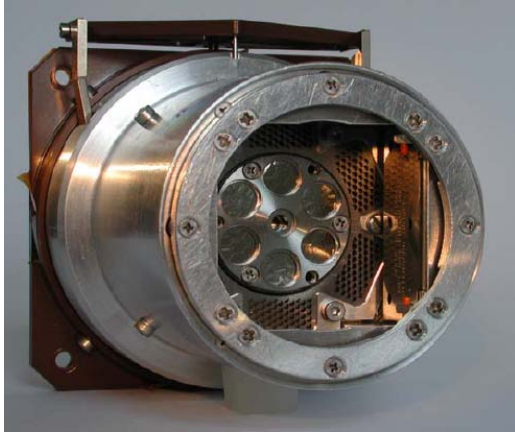


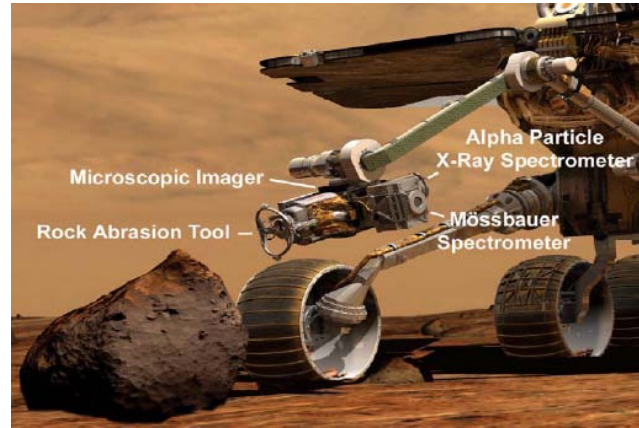Fig.2: APXS flight sensor head with open doors



Fig.3: Mounting position of the APXS on the rover's IDD

## Calibration Samples and Procedures

All instruments built for NASA-MER (two flight units, two flight-spares, and one identical *lab-reference* model, besides a fully functional engineering model) have been calibrated, using 11 complex rock samples, high purity metal oxides (sputter targets), metals and a special *calibration-standard* for cross-calibration. Most rock samples are either certified *geo-standards*, or samples with an independent analysis of their composition, obtained in our own laboratory and/or other laboratories with qualified records. An additional number of about 20 rock samples (equally qualified) and about 40 analytical grade chemical compounds have been used in an extended calibration campaign with the *lab-reference* model only. On the basis of a careful cross-calibration, results can be applied to the flight instruments, as well. The various instruments can be easily cross calibrated by comparing the response, which in this case mainly means elemental peak areas, of each instrument when identical samples are measured under identical conditions. To this end individual cross-calibration factors have been established on an element by element basis, which take care of subtle differences between the instruments in terms of thickness of detector entrance windows and source exit windows, as well as different source strength of the excitation sources.

All samples are in the form of ground powder with grain-sizes of usually less than 100 µm. Some rock samples were also available in the form of cut plates. Agreement of data measured with powders and cut plates is generally good, although there are deviations that require further study (grain-size effects, etc.). Measurements of these samples were performed both under vacuum (at a pressure of less than $10^{-2}$ mbar) and in a simulated Martian atmosphere ($CO_2$ at a pressure of 10 mbar). Special care was taken with respect to a reproducible sample-instrument geometry (flat sample surface; distance error of less than 0.05 mm), and samples were dried in vacuum at 120°C for several hours prior to exposure to the instrument.

## Spectrum Deconvolution (Peak Fitting)

To extract element-specific information (peak intensities), the measured complex spectra must be *deconvoluted*. This is done by performing non-linear least squares fits, using the well-known code MINUIT [4]. The mathematical model, describing the spectral contributions, consists of functions describing the individual peaks of each element (up to 5 lines per element), exponential tailing at the low energy side of the peaks, a background component due to Compton scattering, a general

background component due to Bremsstrahlung, and functions describing the distributions resulting from elastic (Rayleigh -Thomson) and inelastic (Compton) scattering of the exciting x-radiation in the sample. Instead of using the more common Gauss-function to describe the individual peaks, this model uses error functions (integrals of Gauss-functions). This approach has yielded significant improvements, when peaks extend over only a few channels in the spectrum. Parameters of the model functions have been derived in individual fitting procedures with simpler single-element spectra, and are kept fixed relative to one another, when fitting more complex spectra. Inspection of the residua reveals that the agreement between the model and the measured data is usually well within the limits defined by counting statistics.

## Matrix Correction and Derivation of Concentrations

Theoretical x-ray yields have been calculated for all calibration samples, using the computer codes YLD (for alpha-excitation) and XRFY (for x-ray excitation), provided by Campbell et al. [5]. These codes model the physical processes for alpha- and x-ray-excitation (PIXE and XRF), assuming a homogeneous matrix, a smooth surface, and well defined entrance- and exit-angles. From these yields we determined *matrix-factors* that describe the x-ray intensities (per unit concentration) of each element in the matrices of the individual calibration samples, relative to an average intensity (per unit concentration) of the whole set of samples. One of the results of these model calculations was that yields closely correlate with a function of the form $1/(\mu_{in} + \mu_{out})$, where $\mu_{in}$ stands for the mean x-ray absorption coefficient of the matrix for the *incoming* (exciting) radiation (Pu-L lines), and $\mu_{out}$ stands for the mean x-ray absorption coefficient of the matrix for the *outgoing* radiation (Fig. 4).
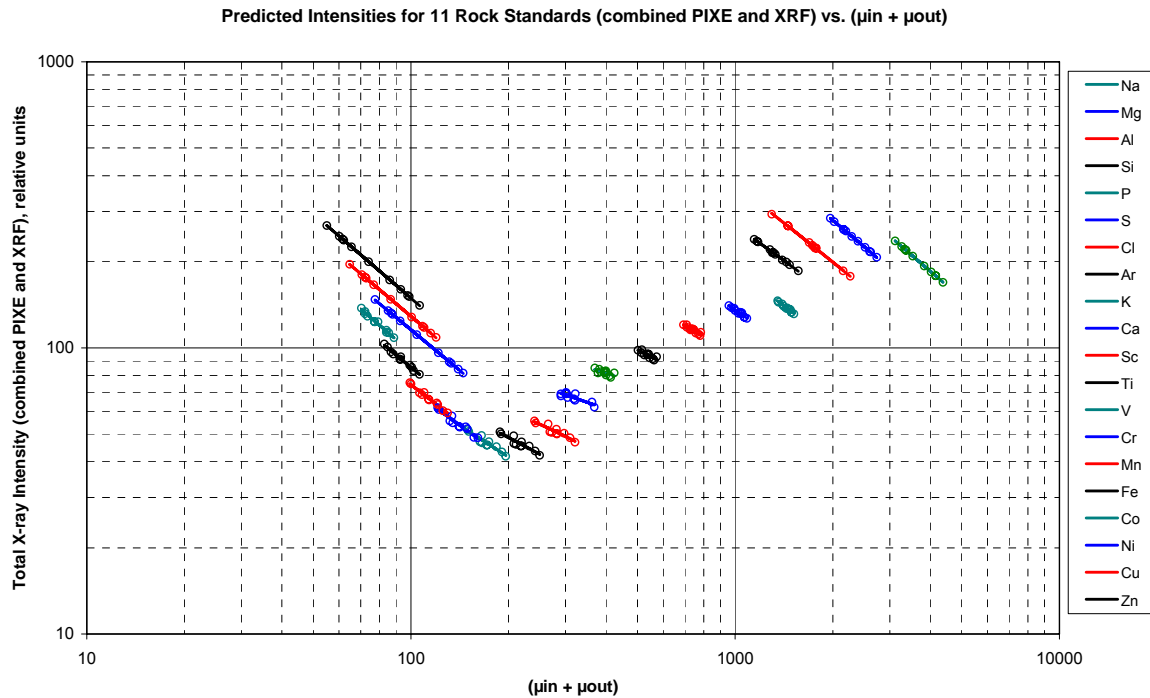


Fig. 4: Predicted x-ray yields for combined excitation by alpha-particles and x-rays from [244]Cm sources in the 11 rock standards used for cross calibrations between the flight instruments and the lab-reference instrument.

This was to be expected for all cases, where x-ray excitation predominates (e.g. Fe). Here, exp -($\mu_{in}$*d) describes the production of x-rays in depth d in the sample by the *incoming* radiation, and exp -($\mu_{out}$*d) the attenuation of the *outgoing* radiation from depth d in the sample. Integration for an infinitely thick sample (from d = 0 to d = ∞) then yields the above form. It was, however, at first a surprise that this form is also applicable to cases, where alpha excitation predominates. The

explanation is that in these cases (Na through ~ Ca) $\mu_{out}$ is much larger than $\mu_{in}$, which means that only x-rays generated in a very shallow layer (1 to 5 µm) can penetrate to the surface. As this layer is also much thinner than the range of alpha particles (~ 30 µm), the decrease of production with depth is small and the dominant factor is $\mu_{out}$. When applying these *matrix-factors* to the measured intensities (peak area intensities obtained from the deconvolution of the spectra), we expected to find a linear relationship between corrected intensities and concentrations. For most samples this is indeed the case. There are, however, *outliers* that we have not yet fully understood. The most obvious reason is that the above assumptions – homogeneous matrix, smooth surface, and well defined entrance- and exit-angles – are certainly not true. In particular, the assumption of homogeneity may be grossly misleading, when certain elements only occur in certain mineral phases, and we have evidence that this is indeed the case for, e.g. phosphorus, which is known to predominantly reside in apatite, and for which matrix-corrected intensities show poorer correlations with *true* concentrations than uncorrected intensities. After the behaviour of phosphorus had become apparent, a pragmatic approach was taken to include such effects: all standards have been subject to a least squares analysis, by which a linear relationship between *true* concentrations and a combination of matrix-corrected and uncorrected intensities of the form {x * corrected + (1-x) * uncorrected} was investigated, which yielded specific values of (0 < x < 1) for each element that appear plausible in the light of their mineralogical occurrences. For samples measured to date this pragmatic approach of *matrix correction* has been applied.

Ultimately, the composition of a sample is derived by converting results for individual elements into stoichiometric oxides (in this case Fe is converted to FeO; if Mößbauer data on the ratio of $Fe^{2+}/Fe^{3+}$ are available, this can be refined to properly partition Fe between FeO and $Fe_2O_3$) and calculating closure to 100 %, neglecting possibly present *invisibles*, like $H_2O$ and $CO_2$. This is done iteratively until convergence is obtained, and also yields information about the geometry (distance), in which the sample was measured.

**Work in Progress**

In the meantime, work continues at the University of Guelph on a more sophisticated model calculation, and first results look very promising: most importantly (and encouragingly), the differences in reduced data obtained by the more sophisticated models and the pragmatic model described above, turn out to be quite small. The more sophisticated model may, however, lend itself to the inclusion of more elaborate algorithms that could eventually include a breakdown of samples into normative minerals and a detailed computation of matrix effects in a mix of different matrices. Another issue to be handled by this model concerns the estimation of *invisibles*, in particular water, from the evaluation of the elastic and inelastic scatter peaks of the exciting x-ray lines. It is anticipated that this model will be completed and tested by the end of 2005, at which time all data (both from calibration standards and from samples on Mars) will be reprocessed and published as – hopefully – final results.

**One last Comment**

Readers, familiar with the problems encountered in XRF analysis of powder samples, may be surprised by the performance of the APXS – in particular with respect to light elements, like Na, Mg, Al and Si. It appears that when using alpha-particles for excitation, paired with a careful calibration, the APXS can render results of a quality far superior to the commonly adopted notion of a *qualitative*, at best *semi-quantitative* nature of such analyses.

**References**

[1]     R. Rieder, R. Gellert, J. Brückner, G. Klingelhöfer, G. Dreibus, A. Yen, and S. W. Squyres, JOURNAL OF GEOPHYSICAL RESEARCH, VOL. 108, NO. E12, 8066, 2003

[2]     Research Institute of Atomic Reactors of the Russian Federation (RIAR) in Dimitrovgrad, Russia; http://www.niiar.ru/

[3]     Ketek GmbH, Munich;   http://www.ketek.net/

[4]     F. James, M. Roos: MINUIT Handbook, CERN, Version 89.12 j; http://wwwasdoc.web.cern.ch/wwwasdoc/minuit/minmain.html

[5]     YLD is a modified version of the PIXE-yield program GUYLS, which is part of the program package for PIXE analysis – GUPIX – available from the University of Guelph; http://pixe.physics.uoguelph.ca/gupix/main/

        XRFY is a program especially written for APXS analysis by John Maxwell to predict x-ray yields from excitation by discrete x-ray lines from radioisotopes.

        Both codes will become available from the University of Guelph as part of a comprehensive package (GUPIX-APXS), especially developed for the analysis of APXS data. This will also include a program for spectrum deconvolution. Anticipated time of completion is end of 2005.